This is a repository copy of *Microstructure and properties of complex concentrated C14–MCr2 Laves, A15–M3X and D8m M5Si3 intermetallics in a refractory complex concentrated alloy*.

Version: Published Version

Article:

Article

Microstructure and Properties of Complex Concentrated C14–MCr$_2$ Laves, A15–M$_3$X and D8$_m$ M$_5$Si$_3$ Intermetallics in a Refractory Complex Concentrated Alloy

Nik Tankov, Claire Utton and Panos Tsakiropoulos *

Department of Materials Science and Engineering, Sir Robert Hadfield Building, The University of Sheffield, Mappin Street, Sheffield S1 3JD, UK; mdpi.nixxu@silomails.com (N.T.); c.utton@sheffield.ac.uk (C.U.)
* Correspondence: p.tsakiropoulos@sheffield.ac.uk

Abstract: Abstract: The refractory complex concentrated alloy (RCCA) 5Al–5Cr–5Ge–1Hf–6Mo–33Nb–19Si–20Ti–5Sn–1W (at.%) was studied in the as-cast and heat-treated conditions. The partitioning of solutes in the as-cast and heat-treated microstructures and relationships between solutes, between solutes and the parameters VEC and $\Delta\chi$, and between these parameters, most of which are reported for the first time for metallic UHTMs, were shown to be important for the properties of the stable phases A15–Nb$_3$X and the D8$_m$ βNb$_5$Si$_3$. The nano-hardness and Young's modulus of the A15–Nb$_3$X and the D8$_m$ βNb$_5$Si$_3$ of the heat-treated alloy were measured using nanoindentation and changes in these properties per solute addition were discussed. The aforementioned relationships, the VEC versus $\Delta\chi$ maps and the VEC, $\Delta\chi$, time, or VEC, $\Delta\chi$, Young's modulus or VEC, $\Delta\chi$, nano-hardness diagrams of the phases in the as-cast and heat-treated alloy, and the properties of the two phases demonstrated the importance of synergy and entanglement of solutes, parameters and phases in the microstructure and properties of the RCCA. The significance of the new data and the synergy and entanglement of solutes and phases for the design of metallic ultra-high temperature materials were discussed.

Keywords: alloy design; refractory metal intermetallic composites; refractory complex concentrated alloys; refractory high-entropy alloys; Nb-silicide-based alloys; C14 laves phase; Nb$_5$Si$_3$ silicide; A15 compound

1. Introduction

New materials are required with capabilities beyond those of the Ni-based super-alloys in order to meet the environmental and performance targets of next-generation aero-engines [1–4]. The toughness property target for the new ultra-high temperature materials (UHTMs) for the "beyond the nickel superalloys era" [5,6] places it in an advantageous position the metallic UHTMs [7]. Currently, the latter are multiphase refractory metal (RM) intermetallic composites (RMICs), e.g., [7–9], and single-phase or multi-phase RM high-entropy alloys (RHEAs) and RM complex concentrated alloys (RCCAs), e.g., [7,10–12]. Some of the multiphase RHEAs and RCCAs also can be classified as RMICs, i.e., RHEAs/RMICs or RCCAs/RMICs, and some RMICs also can be classified as RHEAs or RCCAs, i.e., RMICs/RHEAs or RMICs/RCCAs [12–15] (see Abbreviations). Data about the properties and chemical composition of phases in the said metallic UHTMs is required to improve alloy design and development.

Different approaches utilising different "alloy design landscapes" are used by researchers to design metallic UHTMs; for example, see [12,16–22] for RMICs and [12,23–41] for RHEAs and RCCAs. To obtain a balance of properties or meet a specific property target in metallic UHTMs, (i) sought-after phases are bcc (A2/B2) solid solution(s), M$_5$Si$_3$ silicides, Laves phases and A15 compounds and binary or ternary eutectics with said phases (for example, see [7,8,10,12,23,27,29]) and (ii) appropriate alloying additions are

simple metal and metalloid elements (e.g., Al, B, Ge, Si, Sn), transition metals (TMs) (e.g., Cr, Hf, Ti, Zr) and transition/refractory metals—RMs (e.g., Mo, Nb, Ta, W); for example, see [7,9,10,26,27,30,31,37,39,40].

The aforementioned phases in metallic UHTMs can be "conventional" or "complex concentrated" ("compositionally complex" (CC)) or "high entropy" (HE), depending on their chemical composition [12,42,43] (HEA alloys and HE phases are those alloys and phases where the maximum and minimum concentrations of elements are not above or below, respectively, 35 and 5 at.%, whereas RCCAs alloys and CC phases are those where the maximum and minimum concentrations of elements are above 35% (up to about 40%) and below 5% [10,12,24,28,40]). Also, in alloys with Si addition, the solid solutions can be "normal" or Si-free or Ti-rich, the silicides can be "normal" or Ti (and Hf)-rich, the eutectics can be "normal" or Ti-rich, and the A15 compounds can be rich in Al, Ge or Si, depending on the partitioning of solutes [12,44,45].

In metallic UHTMs, said phases are in synergy and entangled [12]. In the "alloy design landscape" that is "drawn" using the alloy design methodology NICE, which links alloy design with the themes of risk, circular economy, processability, material–environment interactions, sustainability and recyclability, the concepts of synergy, entanglement and self-regulation underpin the design/selection and development of metallic UHTMs [12]. A recent publication demonstrated how synergy and entanglement in a RCCA/RMIC, namely the alloy NT1.2, affected the development of its microstructure, and how the properties (nano-hardness and Young's modulus) of its two stable phases, which were the tetragonal $D8_m$ βNb_5Si_3 and the bcc (A2) solid solution, changed with solute additions [46].

The objective of this work was to study another RCCA/RMIC with the same alloying elements as the alloy NT1.2 but with different stable phases, namely the tetragonal $D8_m$ βNb_5Si_3 and the A15-Nb_3X (X = Al, Ge, Si, Sn) intermetallics, in order to (a) demonstrate the role of synergy and entanglement in the development of microstructure, and thus provide extra experimental evidence for synergy and entanglement in RCCAs in addition to the evidence that was summarised in [12] and the new evidence that was provided in [46]; (b) show how synergy and entanglement affected the nano-hardness and Young's modulus of the stable phases; (c) find out (i) how the properties and parameters VEC (number of valence electrons per atom filled into the valence band) and $\Delta\chi$ (based on electronegativity) changed with each solute element and (ii) whether the changes in the properties and parameters of the silicide depended on it being in synergy not with a bcc (A2) solid solution, as in the case of the RCCA/RMIC alloy NT1.2 [46], but instead with A15-Nb_3X; and (d) provide new data about nano-hardness and Young's modulus and chemical composition of phases that would improve the design and development of metallic UHTMs.

The importance of synergy and entanglement of solutes, parameters and phases in the microstructure and properties of the studied alloy will be demonstrated using relationships between solutes, between solutes and the parameters VEC and $\Delta\chi$ and between these parameters, as well as VEC versus $\Delta\chi$ maps, and VEC, $\Delta\chi$, time, or VEC, $\Delta\chi$, Young's modulus or VEC, $\Delta\chi$, nano-hardness diagrams of the phases in the as-cast and heat-treated alloy, and the properties of the two phases. The significance of the new data and the synergy and entanglement of solutes and phases for the design of metallic ultra-high-temperature materials will be discussed.

2. Experimental

The nominal composition (at.%) of the metallic UHTM of this study was 5Al–5Cr– 5Ge–1Hf–6Mo– 33Nb–19Si–20Ti–5Sn–1W (alloy NT1.1). The alloy was produced as 100 g buttons/ingots using arc melting with a non-consumable tungsten electrode and water-cooled copper crucible, and high-purity elements (purity above 99.99% with the exception of Nb, which had a purity of 99.8%) that were provided in the same form and were used following the same procedure, as described in [33] for the alloy NT1.2.

Samples were mounted in conductive bakelite for the characterization of the alloy. Grinding was carried out using silicon carbide sandpaper with successive grit of P800-P1200-P2400-P4000, and polishing was performed with 1 μm diamond suspension, followed by a final polish using 50 nm diamond suspension. Samples wrapped in Ta foil were heat treated for 100 h and 200 h under Ti gettered inert argon atmosphere at 1500 °C. For the XRD experiments, powder of the alloy, produced using mortar and pestle and filtered through a sieve with 63 μm aperture, was used in a D5000 GA-XRD diffractometer equipped with a Kristallo-Flex 710D X-ray generator (Siemens/Bruker, Billerica, MA, USA) operating at 40 kV and 40 mA, and Bragg–Brentano geometry with 2θ range of 20°–90° and increments of 0.02° per s. ICDD's SIeve+ and PDF-4+ databases were used to analyze the XRD data.

XL30 Philips FEG (Amsterdam, The Netherlands) and InspectF FEG (FEI, Hillsboro, OR, USA) scanning electron microscopes (SEMs), each equipped with a back scatter detector and energy dispersive detector were used for imaging and analysis. The quantitative EDS analysis with elemental standards for all elements and Forsterite (O:45.4%, Mg:34.5%, Si:20.0%) for oxygen was performed on the XL30 using INCA Oxford Instruments analysis software package, with 20 kV per channel [46]. Acquisition duration and processing time were optimised to maintain good spectral resolution with an adequate count rate of 40 kcps and a dead time of up to 20%. Both for EDS and back scatter electron (BSE) imaging, the aperture was set to 3 and the spot size to 5.

Nano-hardness and Young's modulus were measured using a Bruker Hysitron Ti Premier instrument (Siemens/Bruker, Billerica, MA, USA) with a diamond Berkovich indenter. Calibration was performed using an H pattern on a fused quartz sample with a reduced modulus of 69.6 GPa, as instructed by the manufacturer. In the nanoindentation experiments, the indent spacing was set at 5 μm with a serpentine pattern. A load of 10,000 μN was used with 60 s time delay between indents [46].

3. Results and Discussion

3.1. As Cast

The actual chemical composition (at.%) of the as-cast alloy (NT1.1–AC), which was measured using EDS, was (4.4 ± 1)Al–(4.7 ± 0.5)Cr–(4.8 ± 0.3)Ge–(0.9 ± 0.2)Hf–(7 ± 0.3)Mo–(33.5 ± 1.4)Nb–(20.3 ± 2.4)Si–(4.4 ± 0.6)Sn–(19.3 ± 0.4)Ti–(0.9 ± 0.6)W, wherein the parentheses the average concentration and standard deviation value of each element are given. The chemical composition of NT1.1–AC corresponded to that of an RCCA. The alloy can also be classified as an RM(Nb)IC alloy (Nb silicide-based alloy), in other words, the alloy NT1.1–AC was an RCCA/RM(Nb)IC (see Abbreviations).

Similarly, with the alloy NT1.2–AC [46], between the bottom and top of the cast button/ingot of the NT1.1–AC, there was severe macrosegregation of Si (MACSi = C_{max}^{Si} − C_{min}^{Si} = 6.5 at.% versus 6 at.% for NT1.2–AC). Note that high MACSi ($\geq$7 at.%) has been reported for RM(Nb)ICs with the simultaneous addition of Sn with Al, Cr, Hf and Ti (see Table 6 in [47]), and for the Hf and RM free RCCA/RM(Nb)IC alloy OHS1 (MACSi = 6.8 at.%, see the Appendix A for chemical composition) [48] but not for alloys with the simultaneous addition of Ge with Al, Cr, Hf and Ti [49]. The available data for MACSi in metallic UHTMs with Si addition would suggest that Sn and its synergy with other solutes in NT1.1–AC brought about the severe MACSi.

The as-cast microstructure consisted of the βNb_5Si_3 silicide, and the C14–NbCr$_2$-based Laves and A15–Nb$_3$X (X = Al, Ge, Si, Sn) phases (Figure 1a). The Laves and A15 phases formed in-between the silicide grains (Figure 2a,b) and often were part of a eutectic (Figure 2c,d). The eutectic was observed in all parts of the button/ingot and consisted of the Laves and A15 phases, where the A15 exhibited different contrast owing to differences in its <X> =Al + Ge + Si + Sn, Ti, Ge + Sn and Mo + W contents and Sn/Ge ratio (see caption of Figure 2). The average chemical composition of the silicide, Laves, A15-Nb$_3$X (low <X> and Ti content) phases and the eutectic in NT1.1–AC is shown in Table 1. The βNb_5Si_3 silicide was the primary phase that formed at a very high volume fraction (Table 2), and solidification followed with the formation of A15–Nb$_3$X or the eu-

tectic. The "architecture" of the as-cast microstructure was the same in NT1.1–AC and NT1.2–AC (compare Figure 2a with Figure 3a in [46]), and suggested that alloy(s) with composition(s) comparable to those of NT1.1 and NT1.2 [46] would be suitable for directional solidification (DS) processing (see Section 4). Owing to their chemical composition, the aforementioned phases and the eutectic in NT1.1–AC were "complex concentrated" (CC, "compositionally complex").

(**a**)

(**b**)
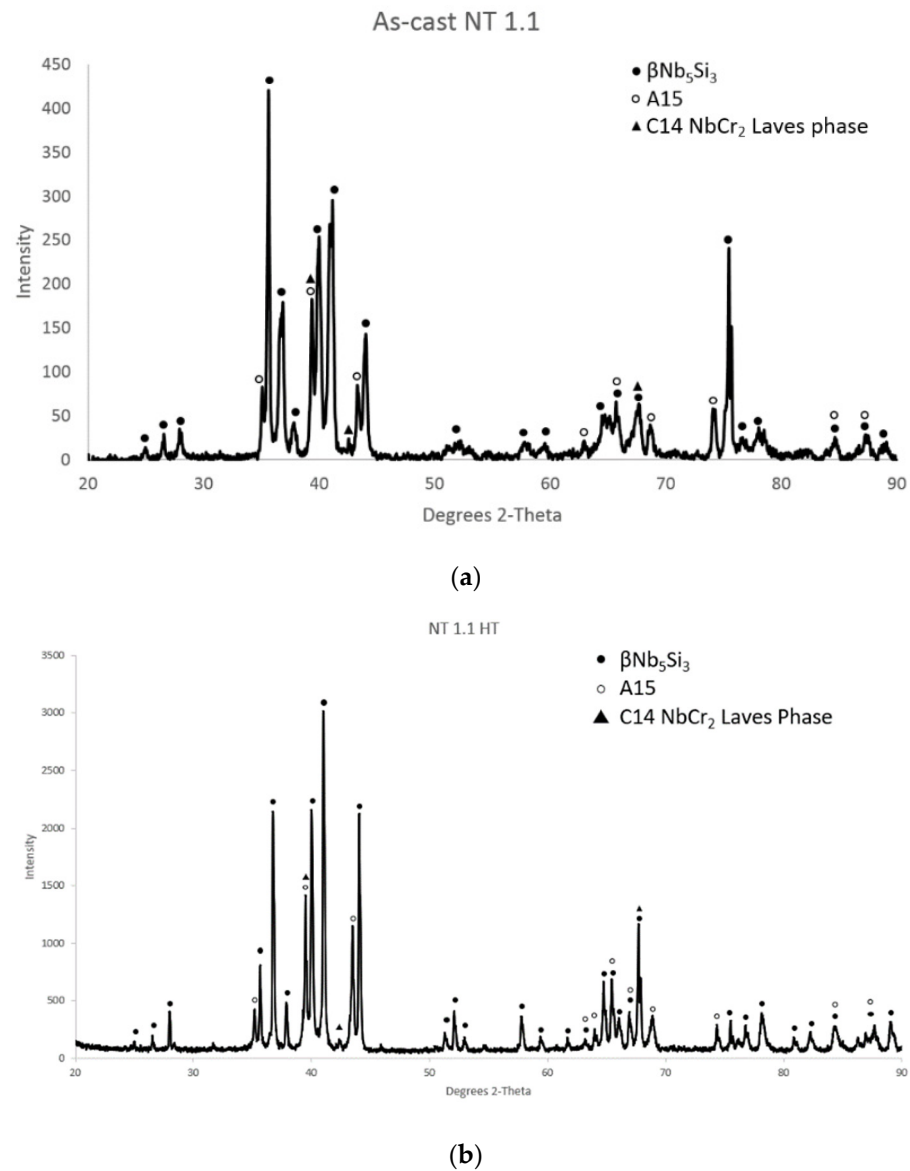
Figure 1. X-ray diffractograms of the as-cast and heat-treated alloy NT1.1. (**a**) NT1.1–AC, (**b**) NT1.1–HT200.
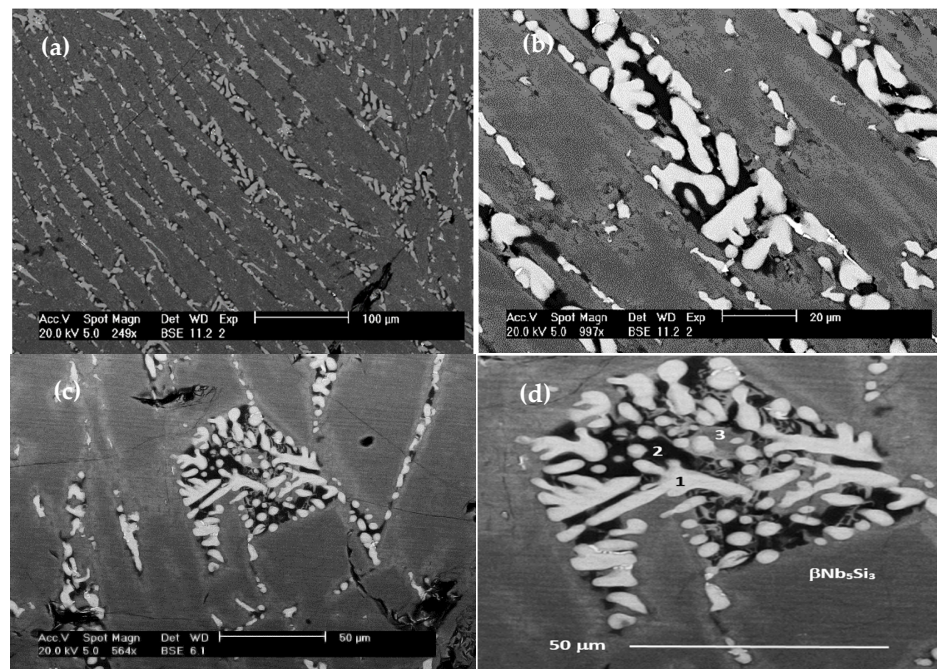
Figure 2. Back scatter electron images of the microstructure of NT1.1–AC. (**a**,**b**) show low and higher magnification images of the microstructure, where the grey phase is the βNb$_5$Si$_3$, the dark phase is the C14–NbCr$_2$-based Laves and the brighter phase is the A15–Nb$_3$X, (**c**) shows microstructure with eutectic and (**d**) shows the magnified eutectic in (**c**), where 1 = A15–Nb$_3$X low <X> (<X> = Al + Ge + Si + Sn), 2 = Laves phase, 3 = A15–Nb$_3$X high <X>. In (**d**), the very thin and bright contrast phase between A15–Nb$_3$X low <X> grains in the bottom left-hand corner of the image is hafnia. Average values for 1, 2 and 3 are as follows: the A15–Nb$_3$X low <X> had <X> = 21.9 at.%, Ti = 19.8 at.%, Ge + Sn = 11 at.%, Sn/Ge = 8, Mo + W = 21.5 at.%, the Laves phase had <Cr> = 58.9 at.%, Ti = 12.4 at.%, Ge + Sn = 2.8 at.%, Al + Cr = 50.8 at.%, Mo + W = 7.2 at.%, and the A15–Nb$_3$X high <X> had <X> = 35 at.%, Ti = 34.4 at.%, Ge + Sn = 21.4 at.%, Mo + W = 5.8 at.%, Sn/Ge = 9.6. <Cr> = Al + Cr + Ge + Si.

Table 1. Chemical composition (at.%, average and standard deviation value) of phases in NT1.1–AC.

Phase	Nb	Ti	Si	Al	Cr	Hf	Mo	W	Sn	Ge
Laves	18.8 ± 0.8	12.4 ± 0.9	6.8 ± 0.7	11.1 ± 1.1	40.3 ± 1.1	1.3 ± 0.2	5.7 ± 0.2	1.6 ± 0.5	1.1 ± 0.4	0.9 ± 0.4
Silicide	37.9	16.8	26.8	2.2	1.4	0.7	5.7	1.7	1.4	5.4
	±1.8	±1.6	±3.0	±0.9	±0.4	±0.2	±0.5	±0.5	±0.6	±0.8
Eutectic	19.1	23.3	3.5	10.1	18.2	0.7	11.1	1.7	11.0	1.3
	±1.8	±2.5	±0.3	±1.1	±3.3	±0.1	±0.4	±0.1	±0.5	±0.1
A15-Nb$_3$X	28.8	19.8	3.6	7.3	7.7	0.3	18.6	2.9	9.7	1.3
	±0.3	±0.7	±0.9	±0.4	±0.4	±0.1	±0.6	±0.4	±0.3	±0.4

Table 2. Volume percentages of phases in the alloy NT1.1.

Phase	NT1.1–AC	NT1.1–HT200
Nb$_5$Si$_3$	78%	80%
A15-Nb$_3$X	14.5%	15.5%
Ti-rich Nb$_5$Si$_3$	-	2%
C14-NbCr$_2$ Laves	5.5%	-
Hafnia	1%	1.5%
Casting defects	1%	1%

The C14–NbCr$_2$-based Laves phase had <Cr> =Al + Cr + Ge + Si + Sn = 60.2 at.%, in agreement with the chemical composition of C14–NbCr$_2$-based Laves phases in RM(Nb)ICs (or Nb silicide-based alloys) [44] and close to the <Cr> content (=57.5 at.%) of the C14–NbCr$_2$-based Laves phase in NT1.2–AC [46]. However, compared with the Laves phase in NT1.2–AC, it was richer in Al + Cr (Al + Cr = 51.4 at.% versus 45.9 at.%) and Mo + W (7.3 at.% versus 3.8 at.%). Also, note that the average chemical composition of the Laves phase in Figure 2d (phase identified with the number 2) was in agreement with the data for the Laves phase in Table 1. The silicide had <Si > =Al + Ge + Si + Sn = 35.8 at.%, in agreement with [50], and its Nb/(Ti + Hf) ratio was 2.17, which is indicative of tetragonal silicide [51], in agreement with the XRD data (Figure 1a). Whereas in NT1.2–AC there was strong partitioning of Ti in the silicide that resulted to Ti-rich Nb$_5$Si$_3$ [46], in NT1.1–AC, the partitioning of Ti was strong only in A15–Nb$_3$X (Figure 2c,d). The partitioning of Ge in the silicide was stronger than that of Sn, in agreement with the silicide in NT1.2–AC [46] and with data for RM(Nb)ICs, RCCAs and RMICs/RCCAs with simultaneous Ge and Sn additions (see [12,46]).

Unlike the NT1.2–AC [46] and many RM(Nb)ICs with eutectics that contain bcc Nb$_{ss}$ solid solution and βNb$_5$Si$_3$ [45], the silicide did not participate in the eutectic in NT1.1–AC. The eutectic had <Si> = Al + Ge + Si + Sn = 25.9 at.%, close to the upper value (=24.3 at.%) of the <Si> content in eutectics with Nb$_{ss}$ and βNb$_5$Si$_3$ [45]. Furthermore, the Mo content of the eutectic in NT1.1–AC decreased as its Si content increased, a trend that is similar to that in eutectics with Nb$_{ss}$ and βNb$_5$Si$_3$ that are formed in RM(Nb)ICs (see Figure 11 in [45]).

The partitioning of Ti in the A15–Nb$_3$X that resulted in the formation of Ti-rich A15–Nb$_3$X, which was observed in this work (Figure 2d), has also been reported for the alloys OHS1 (see Table 1 in [48]) and JZ4 and JZ5 (see Tables S1 and S2 in the Supplemental Materials in [52]). For the alloy compositions, see Table A1 in Appendix A. In all four alloys, i.e., NT1.1, OHS1, JZ4 and JZ5, the Ge and Sn were simultaneously present with Al, Cr, Nb, Si and Ti. In the alloys NT1.1, JZ4 and JZ5, the aforementioned elements were also simultaneously present with Hf, Mo and W, but only the alloys NT1.1 and JZ5 had comparable chemical compositions. In the latter two alloys, even though different phases were present in their microstructures, namely the Nb$_5$Si$_3$, C14–NbCr$_2$-based Laves, A15–Nb$_3$X low <X> and A15–Nb$_3$X high <X> (and Ti-rich) in NT1.1–AC, and the Nb$_5$Si$_3$, Ti-rich Nb$_5$Si$_3$, A15–Nb$_3$X low <X>, A15–Nb$_3$X high <X> (and Ti-rich) and TM$_5$Sn$_2$X (X = Al, Ge, Si) in JZ5–AC [52], the X/Ti ratios and the Mo + W and Ge + Sn contents of the A15–Nb$_3$X were essentially the same (e.g., the A15–Nb$_3$X low <X> had <X> =21.3 at.%, Ti = 19.8 at.%, Mo + W = 21.5 at.%, Ge + Sn = 11 at.% and <X> /Ti = 1.08 in NT1.1–AC, and <X> = 21.6 at.%, Ti = 19.4 at.%, Mo + W = 21 at.%, Ge + Sn = 12.4 at.% and <X> /Ti = 1.11 in JZ5–AC). This is new data and supports the synergy and entanglement of phases in metallic UHTMs; see Section 4 in [12].

There was synergy and intricateness (see Section 4 and Appendix A in [12]) of solutes and parameters in different phases and between phases, and entanglement of the latter (for a discussion of the concepts of synergy and entanglement, see [12]). Note that Al and Si stabilise the C14–NbCr$_2$ Laves phase [53–59]. Below, we shall consider each phase and the eutectic separately. We start with the C14–NbCr$_2$-based Laves phase in NT1.1–AC.

Figure 3 shows relationships between Ti and Al, Cr, Ge, Hf, Mo, Si and Sn. (Note the low concentrations and narrow ranges of the Ge and Hf contents in Figure 3d,g that is included to show the trends of Ti versus Ge and Ti versus Hf.) The Ti concentration of the Laves phase decreased as its Cr, Ge, Si and Hf contents increased, as shown in Figure 3a,d,e,g, and increased as its Al, Sn and Mo contents increased, as shown in Figure 3b,c,h. Also, the Ti concentration in the Laves phase decreased as its <Cr> = Al + Cr + Ge + Si + Sn content increased (Figure 3f). Note that the trends shown in Figure 3d,e are opposite to those shown for the Laves phase in the alloy NT1.2–AC [46], owing to the Laves phase being in synergy and entanglement with different phases in the two alloys.
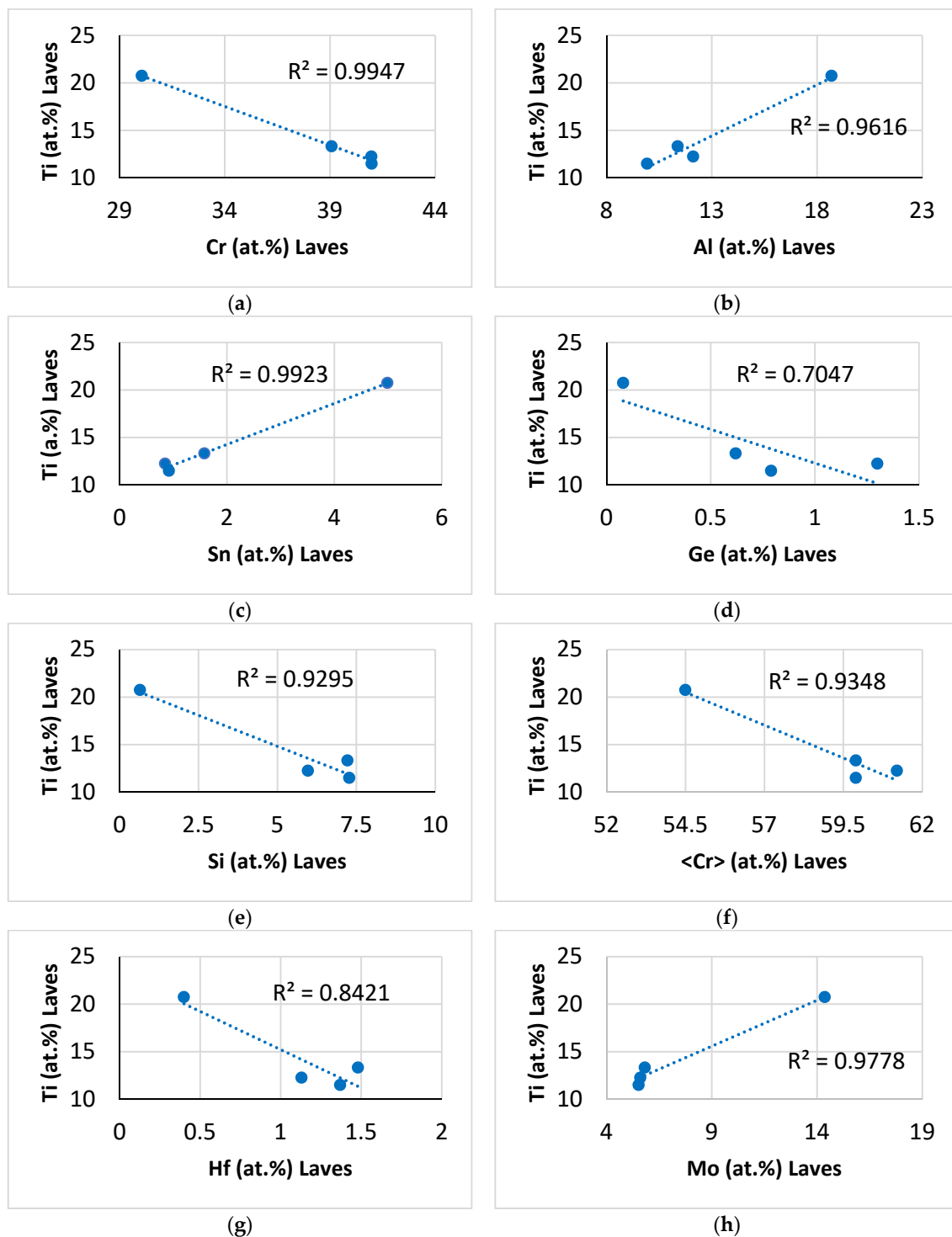
Figure 3. Relationships of Ti with Al, Cr, Ge, Hf, Mo, Si and Sn in the C14–NbCr$_2$-based Laves phase in NT1.1–AC. (**a**) Ti versus Cr, (**b**) Ti vs. Al, (**c**) Ti vs. Sn, (**d**) Ti vs. Ge, (**e**) Ti vs. Si, (**f**) Ti vs. <Cr> =Al + Cr + Ge + Si + Sn, (**g**) Ti vs. Hf and (**h**) Ti vs. Mo.

Other relationships between solutes in the C14–NbCr$_2$-based Laves phase are shown in Figure 4. As the Mo concentration of the Laves phase increased, that of Nb decreased (Figure 4a), but the Ti content increased (Figure 3h). The increase in the Cr concentration was accompanied by a decrease in the Al and Sn contents (Figure 4b,d) and an increase in the Si and Ge contents (Figure 4c,e), whereas the Si and Sn concentrations in the Laves

phase, respectively, decreased and increased with increasing Al content (Figure 4f,g). The concentration of Sn deceased as the Laves phase became richer in Si (Figure 4h).
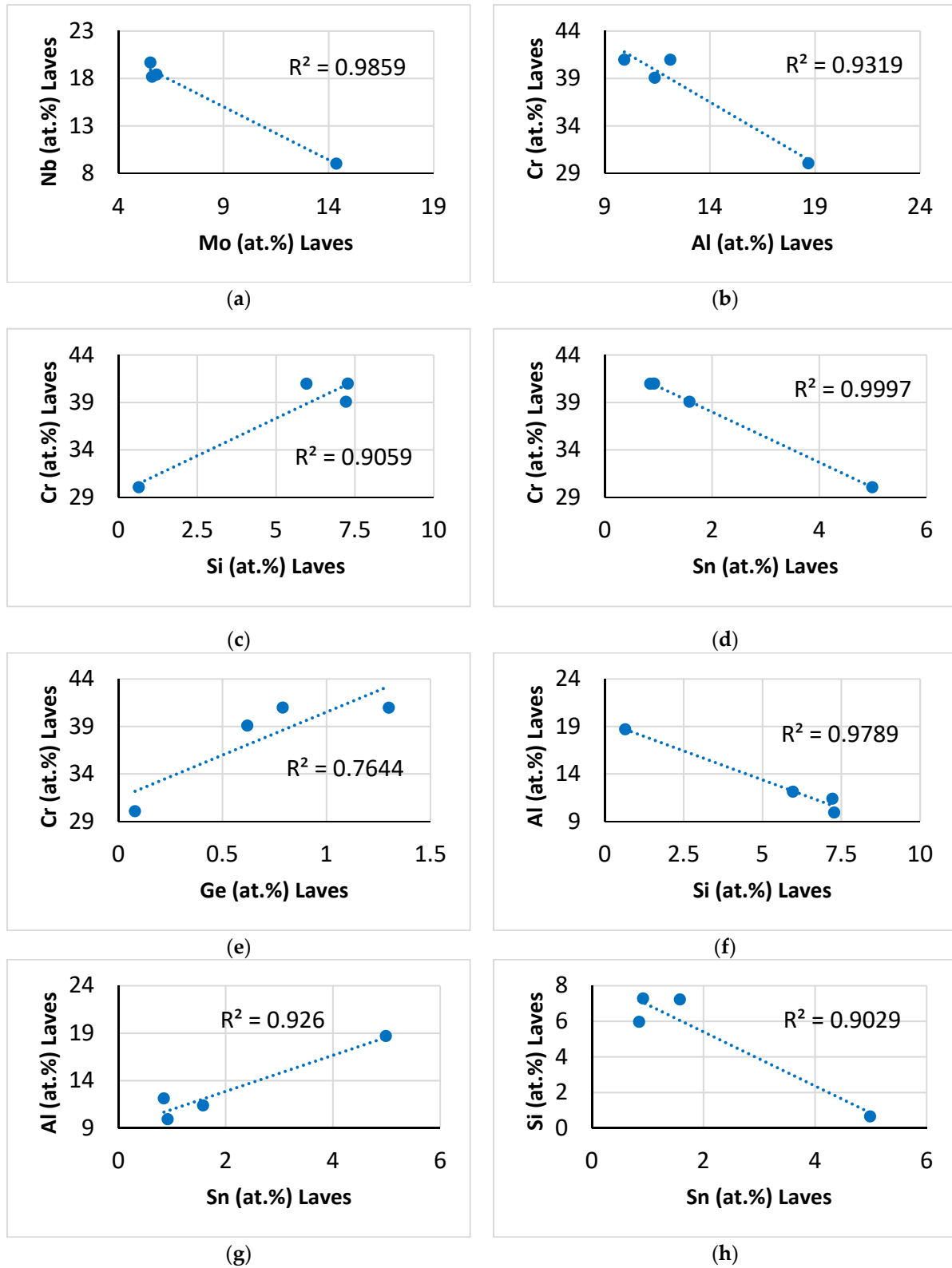
Figure 4. Relationships between solutes in the C14–NbCr$_2$ based Laves phase in NT1.1–AC. (**a**) Nb versus Mo, (**b**) Cr vs. Al, (**c**) Cr vs. Si, (**d**) Cr vs. Sn, (**e**) Cr vs. Ge, (**f**) Al vs. Si, (**g**) Al vs. Sn, (**h**) Si vs. Sn.

Relationships between the parameters VEC and $\Delta\chi$ of the C14–NbCr$_2$-based Laves phase with its Al, Cr and Si solutes are shown in Figure 5. The aforementioned parameters were calculated as described in [44]. The parameter VEC increased as the Cr and Si contents increased (Figure 5a,c) and decreased with increasing Al content (Figure 5b), whereas the parameter $\Delta\chi$ exhibited the opposite trends with the same solutes (Figure 5d–f). Finally, the relationship between the parameters VEC and $\Delta\chi$ of the Laves phase is shown in Figure 6. The absolute value of $\Delta\chi$ (i.e., $|\Delta\chi|$) increased with increasing VEC.
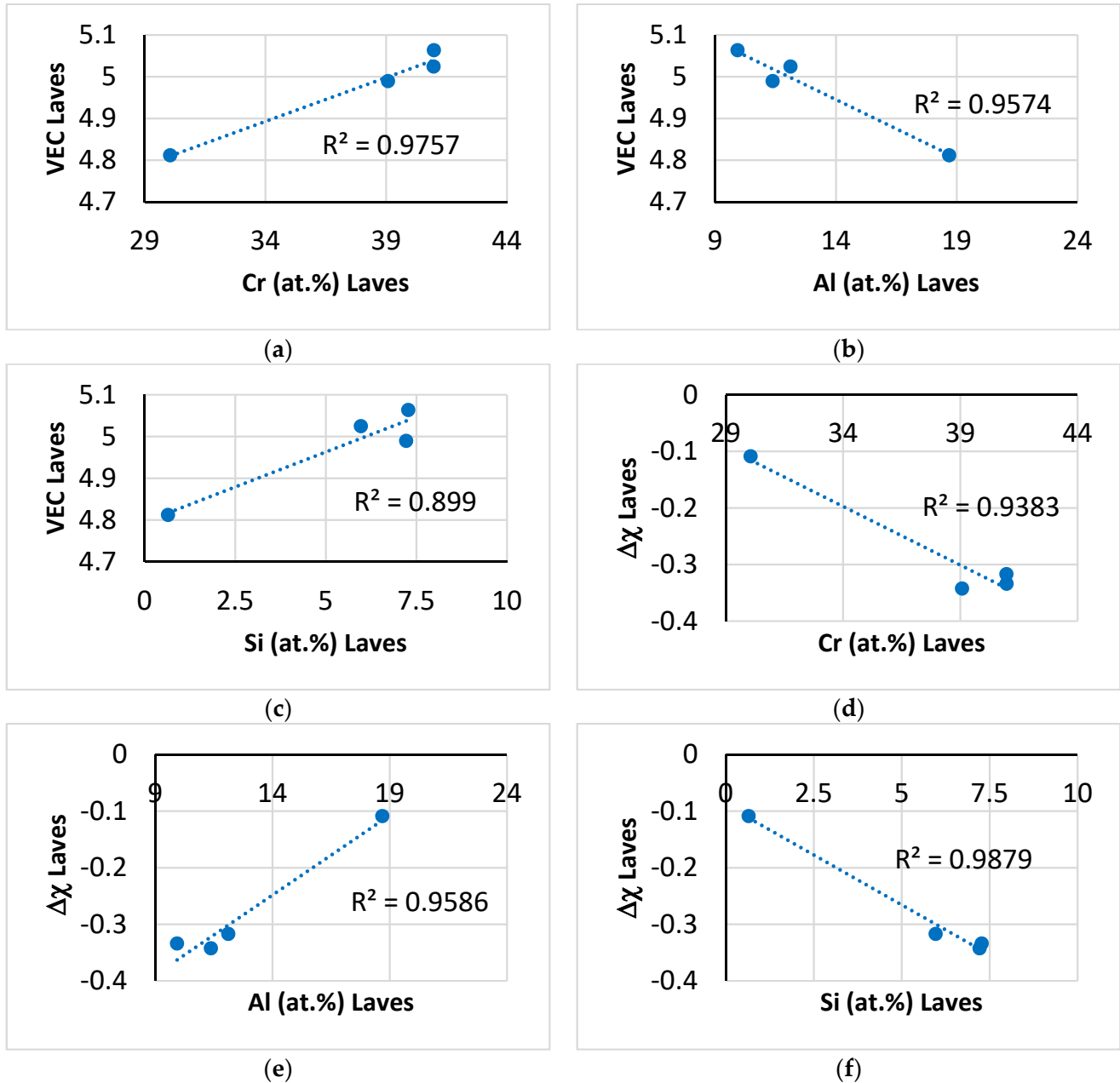
Figure 5. Relationships between the solutes Al, Cr and Si and the parameters VEC and $\Delta\chi$ in the C14–NbCr$_2$-based Laves phase in NT1.1–AC. (**a**) VEC versus Cr, (**b**) VEC vs. Al, (**c**) VEC vs. Si, (**d**) $\Delta\chi$ vs. Cr, (**e**) $\Delta\chi$ vs. Al, (**f**) $\Delta\chi$ vs. Si.
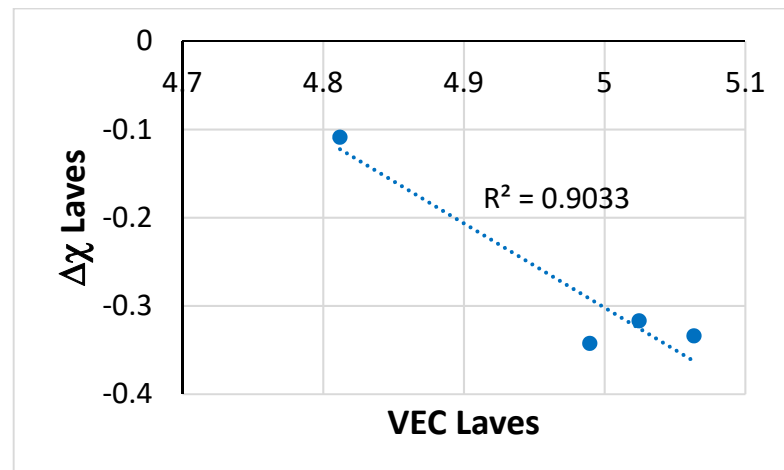
Figure 6. Map of the parameters $\Delta\chi$ and VEC of the C14–NbCr$_2$-based Laves phase in NT1.1–AC.

The synergy and intricateness of solutes in the Laves phase are shown by the data in Figures 3–6. For example, as the Laves phase became richer in Ti its Cr content decreased (Figure 3a), and its VEC and |$\Delta\chi$| values decreased (Figure 5a,d and Figure 6), this allowed more Al in the Laves (Figure 4b) and, in turn, more Sn (Figure 4g) but less Si (Figure 4f). The increase in Al content "went hand in hand" with the increase in the Ti content (Figure 3b) and Ti "pulled in" more Sn (Figure 3c) and Mo (Figure 3h) and "pushed out" Ge (Figure 3d), Hf (Figure 3g) and Si (Figure 3e).

This paper presents for the first time new data for relationships between solutes in the C14–NbCr$_2$-based Laves phase in a metallic UHTM, namely Figure 3b,g,h (compare with [46]), and Figure 4a–c,f–h (see [60]), and between parameters and solutes, namely Figure 5b,c,e,f (see [44]). The aforementioned new data complement the data for relationships between solutes and between parameters and solutes in the C14–NbCr$_2$-based Laves phase that our research group presented for RMICs, also for the first time since 2018 (see [44,60]).

Next, we consider the silicide. Relationships between solutes in the βNb$_5$Si$_3$ are shown in Figure 7. The increase in the Ti concentration in the silicide was accompanied by increases in the concentrations of Cr, Ge, Sn, Al and Mo (Figure 7a–e); in other words, we could say that Ti "pulled in" with it in the silicide the aforementioned elements (see [46]). The same can be said for Cr, which also "pulled in" with it in the silicide the Ge, Al and Sn (Figure 7f–h) that substituted Si in the silicide [61]. Figure 7 is another example of the synergy and intricateness of solutes in an intermetallic, namely the βNb$_5$Si$_3$, in a RCCA/RMIC.

Relationships between the parameters VEC and $\Delta\chi$ of the βNb$_5$Si$_3$ and solutes in NT1.1–AC are shown in Figures 8 and 9. The aforementioned parameters were calculated as described in [61]. With increasing Al, Cr, Ge, Mo, Sn and Ti concentrations in the silicide, the parameters VEC and $\Delta\chi$, respectively, decreased (Figure 8) and increased (Figure 9). Figures 8 and 9 are new examples of the synergy of parameters and solutes in an intermetallic, namely the βNb$_5$Si$_3$, in a RCCA/RMIC.

The relationship between the parameters VEC and $\Delta\chi$ of the βNb$_5$Si$_3$ in NT1.1–AC is shown in Figure 10. Figure 10b, which includes data for the binary (unalloyed) βNb$_5$Si$_3$, should be compared with the data for the <u>B-free</u> silicide in Figure 6 in [60]. The comparison shows that the same trend was followed for the alloyed silicide in NT1.1–AC. This paper presents for the first time new data for relationships between solutes in the βNb$_5$Si$_3$, namely Figure 7e–h (see [60,61]) and between parameters of βNb$_5$Si$_3$ and solutes, namely Figure 8a–c,e,f and Figure 9a–c,e,f (see [45,60,61]). The aforementioned new data complement the data for relationships between solutes and between parameters and solutes in the Nb$_5$Si$_3$ silicide that our research group presented for RMICs, also for the first time since 2018 (see [61]).
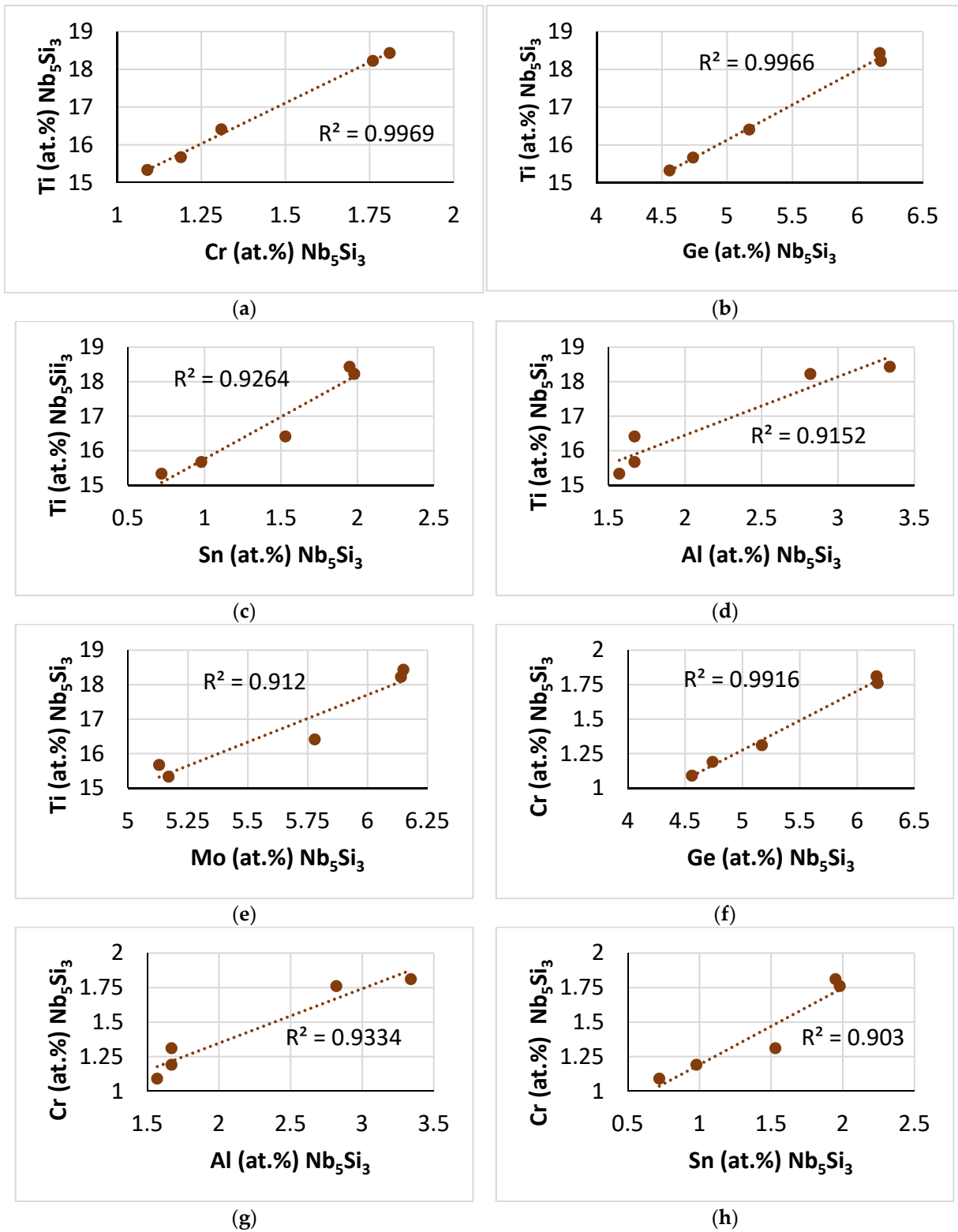
Figure 7. Relationships between solutes in βNb$_5$Si$_3$ in NT1.1–AC. (**a**) Ti versus Cr, (**b**) Ti vs. Ge, (**c**) Ti vs. Sn, (**d**) Ti vs. Al, (**e**) Ti vs. Mo, (**f**) Cr vs. Ge, (**g**) Cr vs. Al, (**h**) Cr vs. Sn.
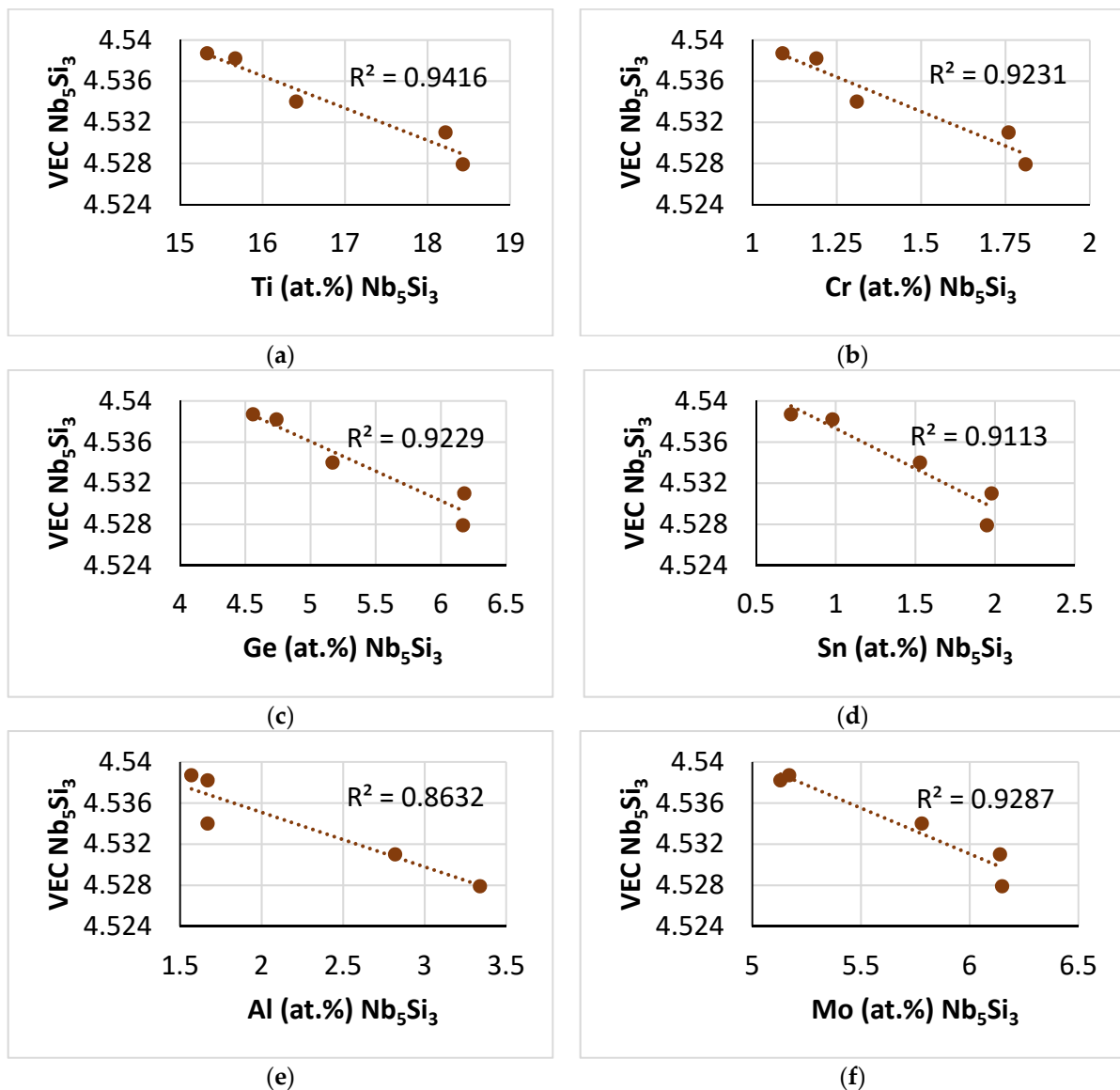
Figure 8. Relationships between the parameter VEC of βNb$_5$Si$_3$ and solutes in the silicide in NT1.1–AC. (**a**) VEC versus Ti, (**b**) VEC vs. Cr, (**c**) VEC vs. Ge, (**d**) VEC vs. Sn, (**e**) VEC vs. Al, (**f**) VEC vs. Mo.

To the authors' knowledge, this is also the first time that such comprehensive data for the βNb$_5$Si$_3$ has been presented for the solutes (Figure 7) and parameters (Figures 8–10) for a M$_5$Si$_3$ silicide in a RCCA/RMIC. These data supplement the new data for the βNb$_5$Si$_3$ that was reported for the alloy NT1.2 in [46]. The two sets of data together with the data in [60,61] have enhanced the capabilities of the alloy design methodology NICE [62] for the development of metallic UHTMs and confirm that the "alloy design landscape", which was discussed in Section 4 in [12], is a "landscape" *in statu nascendi* (in a state of being born).

Relationships between solutes in A15–Nb$_3$X are shown in Figure 11. As the A15–Nb$_3$X became richer in Sn its Nb and Mo contents decreased (Figure 11b,d) and its Al, Ge and Ti concentrations increased (Figure 11f,g,i). Also, the concentrations of Mo and Nb in A15–Nb$_3$X decreased with increasing Ge content (Figure 11a,c,e), but the concentration of Ti increased (Figure 11j). The increase in the Al content of the A15–Nb$_3$X was accompanied by a decrease in its Cr concentration (Figure 11h).
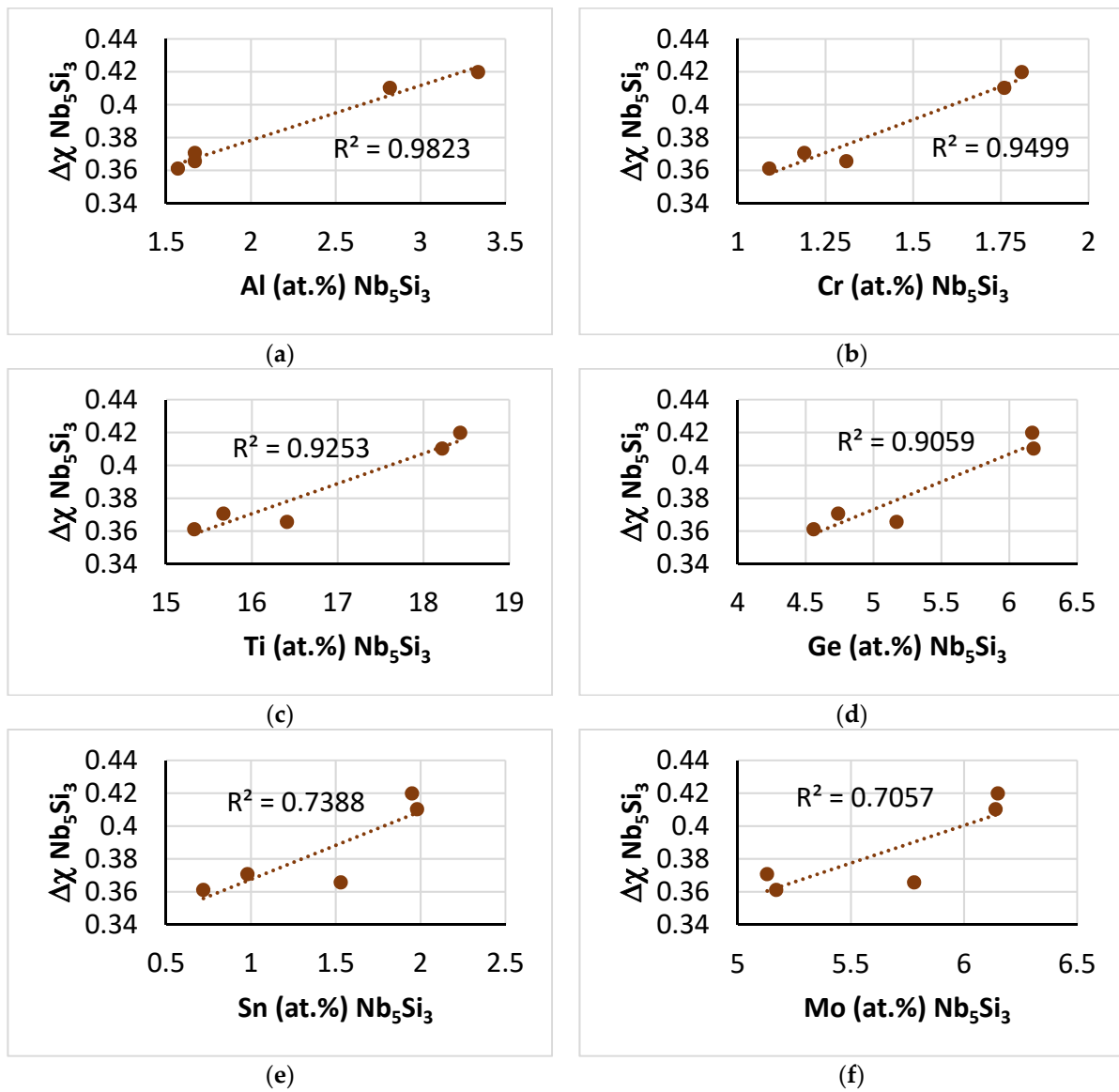
Figure 9. Relationships between the parameter Δχ of βNb$_5$Si$_3$ and solutes in the silicide in NT1.1–AC. (**a**) Δχ versus Al, (**b**) Δχ vs. Cr, (**c**) Δχ vs. Ti, (**d**) Δχ vs. Ge, (**e**) Δχ vs. Sn, (**f**) Δχ vs. Mo.
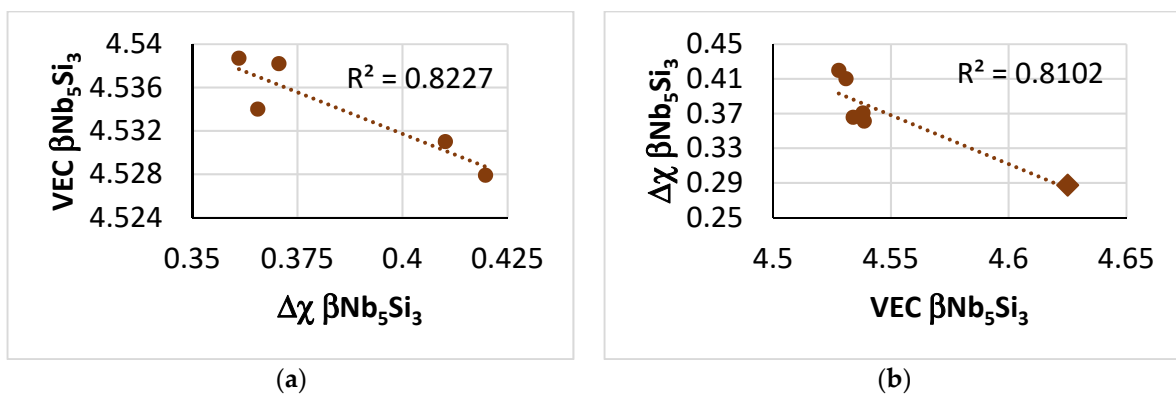
Figure 10. Maps of the parameters VEC and Δχ of the alloyed βNb$_5$Si$_3$ in NT1.1–AC. (**a**) VEC versus Δχ, (**b**) Δχ vs. VEC with data (diamond) for the binary (unalloyed) βNb$_5$Si$_3$.
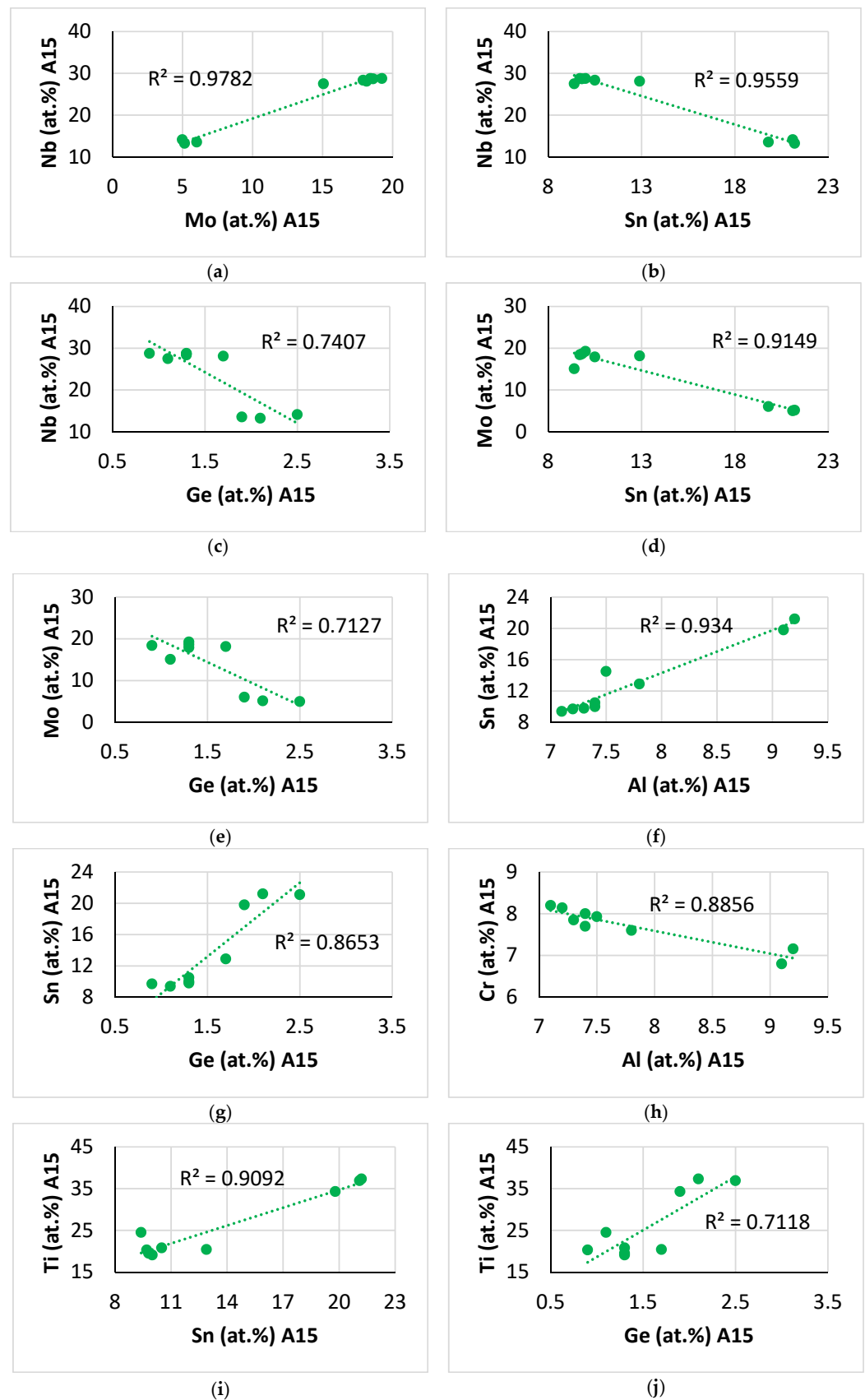
Figure 11. Relationships between solutes in A15–Nb$_3$X (X = Al, Ge, Si, Sn) in NT1.1–AC. (**a**) Nb versus Mo, (**b**) Nb vs. Sn, (**c**) Nb vs. Ge, (**d**) Mo vs. Sn, (**e**) Mo vs. Ge, (**f**) Sn vs. Al, (**g**) Sn vs. Ge, (**h**) Cr vs. Al, (**i**) Ti vs. Sn, (**j**) Ti vs. Ge.

Relationships between the parameters VEC and Δχ of the A15–Nb₃X with Ge, Mo, Nb and Sn are shown in Figures 12 and 13, respectively. The aforementioned parameters were calculated as described in [44]. The parameters VEC and Δχ increased with increasing Mo and Nb concentrations (Figure 12a,b and Figure 13a,b) and decreased with increasing Ge and Sn concentrations (Figure 11c,d and Figure 13c,d).
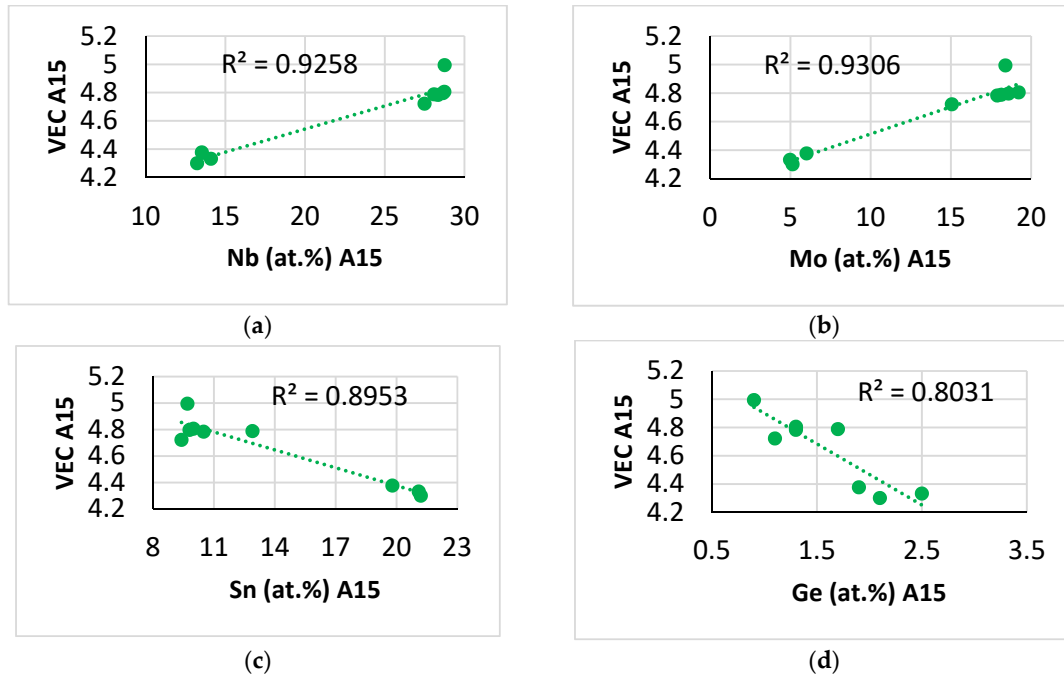
Figure 12. Relationships between the parameter VEC of A15–Nb₃X and solutes in NT1.1–AC. (**a**) VEC versus Nb, (**b**) VEC vs. Mo, (**c**) VEC vs. Sn, (**d**) VEC vs. Ge.
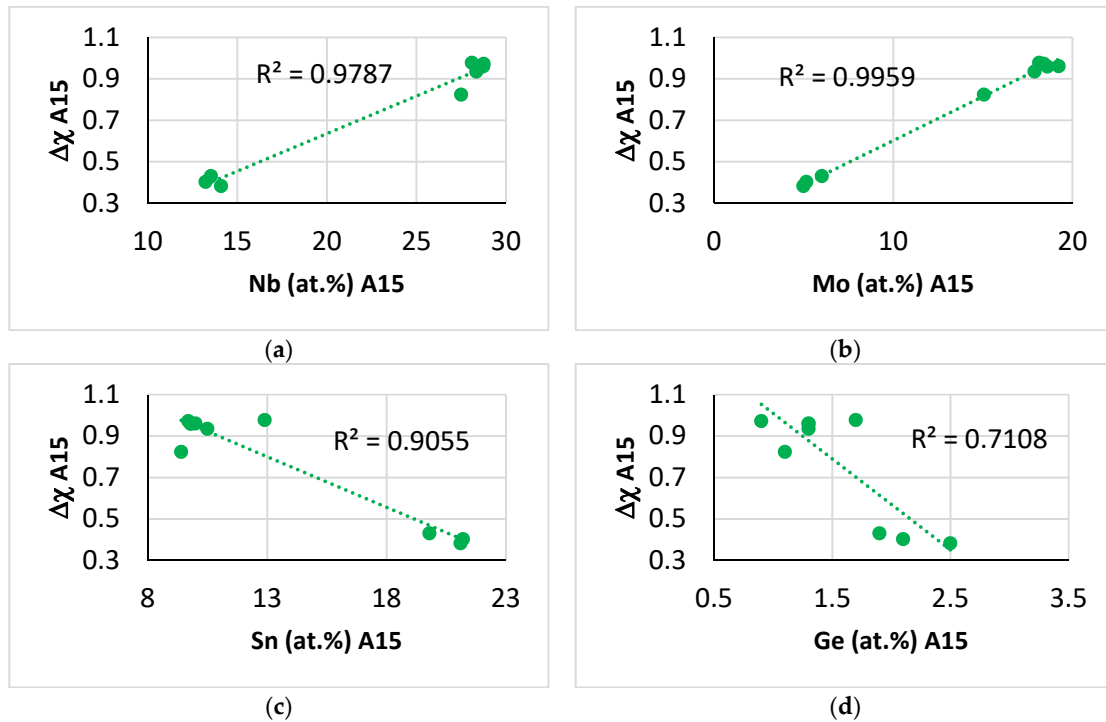
Figure 13. Relationships between the parameter Δχ of A15–Nb₃X and solutes in NT1.1–AC. (**a**) Δχ versus Nb, (**b**) Δχ vs. Mo, (**c**) Δχ vs. Sn, (**d**) Δχ vs. Ge.

The relationship between the parameters VEC and $\Delta\chi$ of the A15–Nb$_3$X is shown in Figure 14. This paper presents for the first time new data for relationships between solutes in the A15–Nb$_3$X, namely Figure 11, (see [44,47]) and between parameters of A15–Nb$_3$X and solutes, namely Figures 12 and 13 (see [44,47,60]). The aforementioned new data complements the data for relationships between solutes and between parameters and solutes in the A15–Nb$_3$X that our research group presented for RMICs, also for the first time since 2018 (see [44,60]).
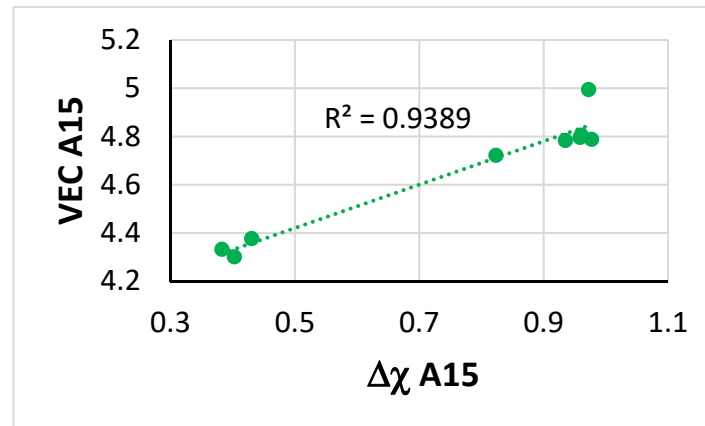
Figure 14. Map of the parameters VEC and $\Delta\chi$ of A15–Nb$_3$X in NT1.1–AC.

To the authors' knowledge, this is the first time that such comprehensive data for the A15–Nb$_3$X have been presented for the solutes (Figure 11) and parameters (Figures 12–14) for an A15 compound in a RCCA/RMIC. These data supplement the data for A15 compounds in [44]. The two sets of data together with the data in [47,60] have increased the capabilities of the alloy design methodology NICE for the design [62] and development of metallic UHTMs [12].

Relationships between solutes and between solutes and the parameters VEC and $\Delta\chi$ of the eutectic are shown in Figure 15. The said parameters were calculated as discussed in [45,63]. The Al and Cr concentrations in the eutectic increased as its Ti content decreased (Figure 15a,b), which increased the VEC parameter (Figure 15c). The parameter $\Delta\chi$ of the eutectic decreased as its <Si> = Al + Ge + Si + Sn content increased (Figure 15d).

This paper presents for the first time new data for relationships between solutes and between parameters and solutes for a eutectic of the A15–Nb$_3$X and C14–NbCr$_2$ based Laves phase, namely Figure 15, in a metallic UHTM. The aforementioned new data complements the data for relationships between solutes and between parameters and solutes in eutectics with bcc (A2) solid solution (Nb$_{ss}$) and βNb$_5$Si$_3$ that our research group presented for RMICs, also for the first time since 2018 (see [45]). To the authors' knowledge, this is the first time that such data for a eutectic of the A15–Nb$_3$X- and C14–NbCr$_2$-based Laves phase in a RCCA/RMIC have been presented in the literature and supplements the data for eutectics in RM(Nb)ICs and RCCAs/RMICs (see [45,60]).

The map of the parameters VEC and $\Delta\chi$ of the phases in NT1.1–AC is shown in Figure 16. The map shows clear correlations ($R^2 > 0.87$) between phases (see figure caption) and confirms their synergy and entanglement (see Section 4 in [12]) in the microstructure of NT1.1–AC. The synergy of solutes and phases, as well as their entanglement, is further supported by relationships between solutes in different phases, examples of which are shown in Figure 17. The latter shows that as the Al and Ti concentrations in the A15–Nb$_3$X increased those of Al and Ti in βNb$_5$Si$_3$ decreased (Figure 17a,b), that a decrease in the Al content of the silicide was accompanied by an increase in the Cr concentration in the A15–Nb$_3$X (Figure 17c), and that the Al concentration in the C14–NbCr$_2$-based Laves phase increased with that in the A15–Nb$_3$X high <X> (Figure 17d), whereas as Ti and Cr

concentrations in the A15–Nb_3X high <X> increased, those in the C14–$NbCr_2$-based Laves phase decreased (Figure 17e,f).

(a)

(b)

(c)

(d)
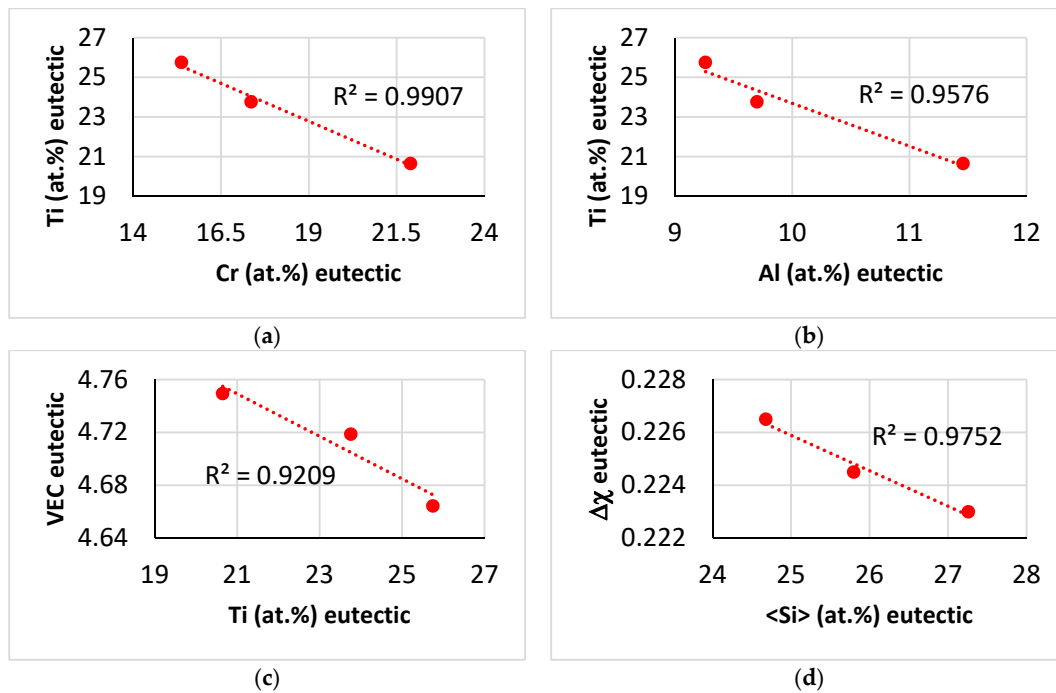
Figure 15. Relationships between solutes and between parameters and solutes for the eutectic in NT1.1–AC. (**a**) Ti versus Cr, (**b**) Ti vs. Al, (**c**) VEC vs. Ti, (**d**) Δχ vs. <Si> = Al + Ge + Si + Sn.
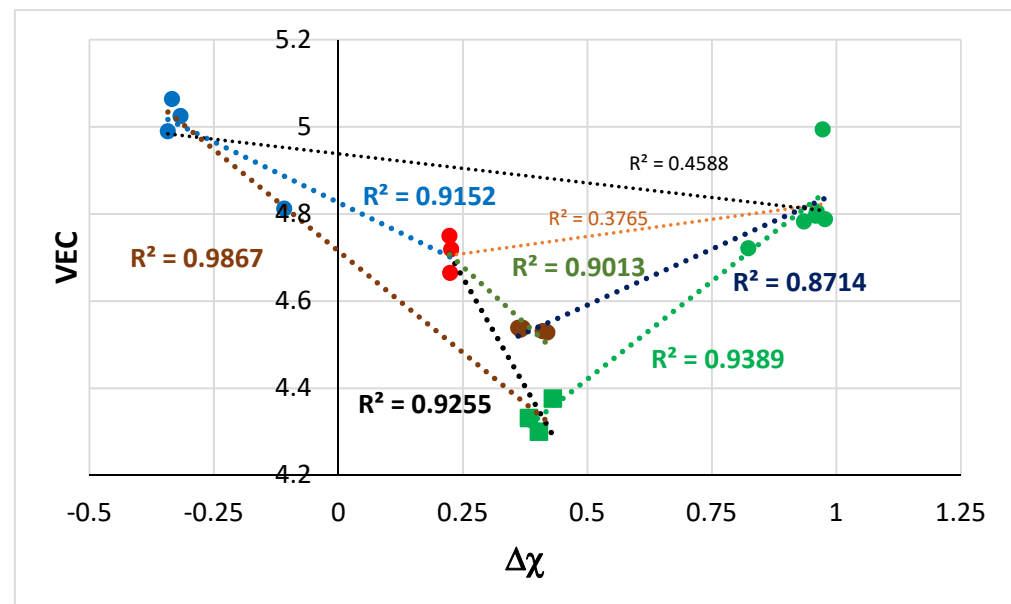
Figure 16. Map of the parameters VEC and Δχ of the phases in NT1.1–AC. Colours as follows: blue, C14–$NbCr_2$-based Laves phase; green, A15–Nb_3X; brown, $βNb_5Si_3$; red, eutectic, squares for A15–Nb_3X with high <X> value (and Ti-rich). R^2 = 0.9867 for the relationship between C14–$NbCr_2$-based Laves phase and A15–Nb_3X high <X>, R^2 = 9389 for A15–Nb_3X high <X> and low <X> (see Figure 14), R^2 = 0.9255 for eutectic and A15–Nb_3X high <X>, R^2 = 0.9152 for C14–$NbCr_2$-based Laves phase and eutectic, R^2 = 0.9013 for $βNb_5Si_3$ and eutectic, R^2 = 0.8714 for $βNb_5Si_3$ and A15–Nb_3X low <X>, R^2 = 0.4588 for C14–$NbCr_2$-based Laves phase and A15–Nb_3X low <X>, R^2 = 0.3765 for eutectic and A15–Nb_3X low <X>. Note that the same colours were used for the data of the phases in Figures 3–16. <X> = Al + Ge + Si + Sn.
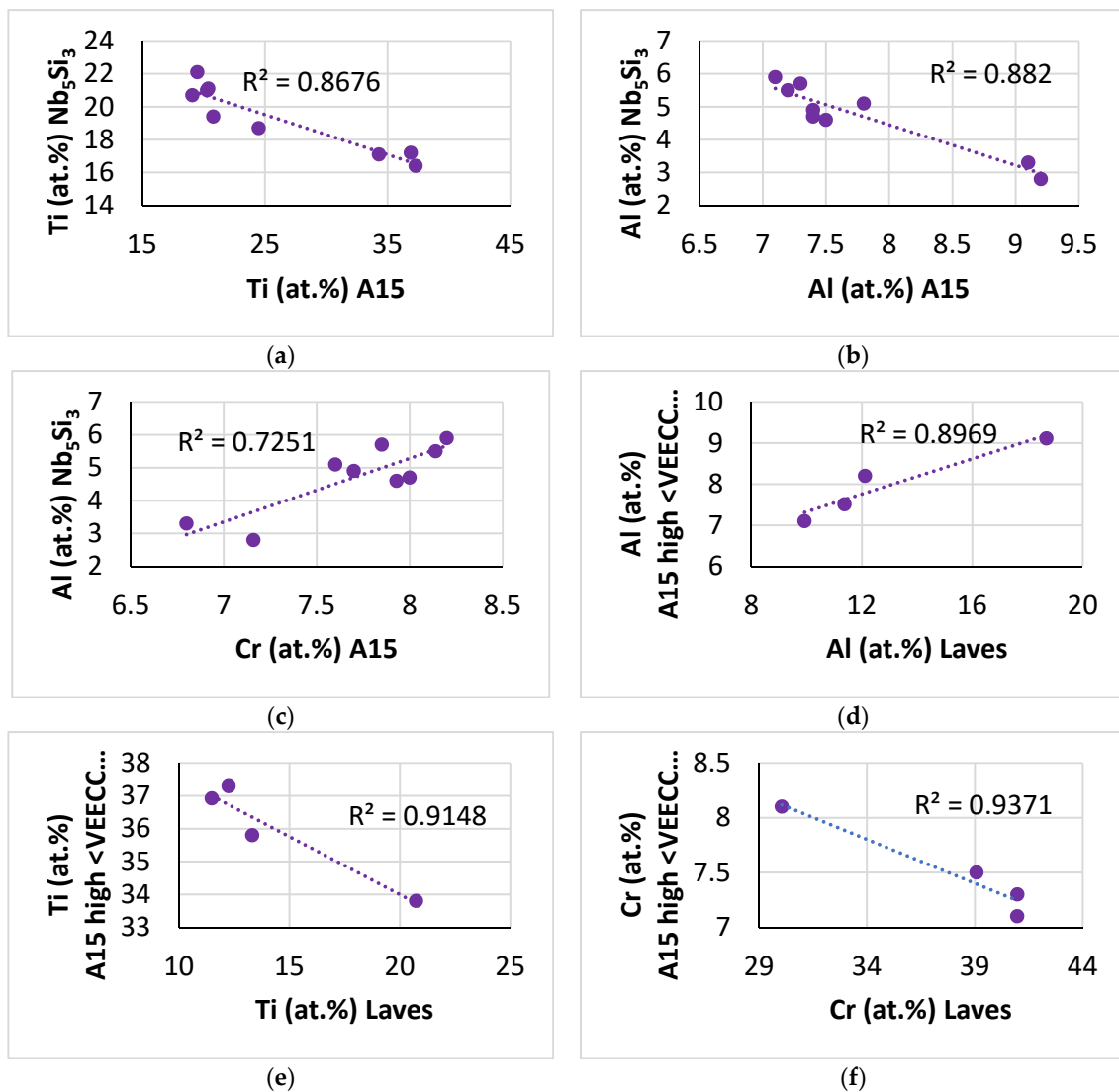
Figure 17. Relationships between solutes in βNb_5Si_3-, A15-Nb_3X- and C14 $NbCr_2$-based Laves in NT1.1–AC. (**a**) Ti in silicide versus Ti in A15, (**b**) Al in silicide vs. Al in A15, (**c**) Al in silicide vs. Cr in A15, (**d**) Al in A15 high <X> vs. Al in Laves, (**e**) Ti in A15 high <X> vs. Ti in Laves, (**f**) Cr in A15 high <X> vs. Cr in Laves.

As we discussed earlier, the βNb_5Si_3 was the primary phase, and solidification continued with the A15–Nb_3X and the eutectic of the A15–Nb_3X- and C14–$NbCr_2$-based Laves phases. As the concentration of Ti increased in the silicide, so did the concentrations of Al (Figure 7d), Cr (Figure 7g), Sn (Figure 7h) and Ge (Figure 7f), the parameters VEC and $\Delta\chi$ of the silicide, respectively, deceased and increased (Figure 8c,d) and (Figure 9d,e) with Ge and Sn contents, whereas in the A15, the concentrations of Ti (Figure 17a) and Al (Figure 17b) decreased, as did the concentrations of Sn (Figure 11f,i), of Ge (Figure 11g) and the parameters VEC and $\Delta\chi$ of the A15–Nb_3X (Figure 12c,d and Figure 13c,d, respectively), but the Cr content increased (Figure 11h). The aforementioned trends in relationships between solute concentrations and between parameters and solute concentrations are examples of the synergy of solutes and parameters in the βNb_5Si_3 and A15–Nb_3X intermetallics, and of the synergy and entanglement of the two phases (abovementioned figures and Figure 16).

Also, there was synergy and entanglement between the C14–$NbCr_2$-based Laves and the A15–Nb_3X high <X> phases (Figures 16 and 17d–f). In the Laves phase, an increase in the Ti concentration was accompanied by (i) an increase in the Al content (Figure 3b), and a decrease and increase, respectively, in the parameters VEC (Figure 5b) and $\Delta\chi$ (Figure 5e)

and (ii) a decrease in the Cr content (Figure 3a) and an increase and decrease, respectively, in the parameters VEC (Figure 5a) and $\Delta\chi$ (Figure 5d). The decrease in Cr in the Laves phase was linked (iii) with an increase in the Si content (Figure 4c) and with an increase and decrease, respectively, in the parameters VEC (Figure 5c) and $\Delta\chi$ (Figure 5f), with an increase in the Ge (Figure 4e) concentration and decrease in the Sn content (Figure 4d).

To the authors' knowledge, this is the first time that correlations between $C14–NbCr_2$ Laves, $A15–Nb_3X$, βNb_5Si_3 and eutectic of $A15–Nb_3X$ and $C14–NbCr_2$ Laves in a RCCA/RMIC are shown in a phase map based on the parameters VEC and $\Delta\chi$ (Figure 16). Note that correlations between bcc (A2) solid solution, $C14–NbCr_2$-based Laves phase and βNb_5Si_3 silicide were also shown for the first time recently in [46] in a phase map based on the same parameters (see Figure 13 in [46]) for a RCCA/RMIC of comparable chemical composition. The maps in Figure 16 of this work and Figure 13 in [46] complement parameter maps of phases in metallic UHTMs and improve the design of metallic UHTM materials or material systems [12,46,60,62,64]. The aforementioned phase maps, together with parameter maps of alloys [60,63] and of bond coat alloys for environmental coatings [64], add to the capabilities of the alloy design methodology NICE [62] and "synergistic metallurgy" (see Section 7 in [12]) regarding the development of metallic UHTMs.

3.2. Heat Treated

After the heat treatments for 100 h and 200 h at 1500 °C, the microstructure of NT1.1–HT consisted of the βNb_5Si_3 silicide and $A15–Nb_3X$ compound, as shown in Figure 1b, which shows the diffractogram after the 200 h heat treatment. The actual chemical composition of NT1.1–HT200, which was measured using EDS, was (4.1 ± 0.7)Al–(4.5 ± 0.3)Cr–(4.9 ± 0.3)Ge–(0.9 ± 0.2)Hf–(7.2 ± 0.3) Mo–(33.8 ± 0.9)Nb–(19.9 ± 1.6)Si–(4.4 ± 0.5)Sn–(19.4 ± 0.2)Ti–(0.9 ± 0.4)W and was close to that of the as-cast alloy. The chemical composition of NT1.1–HT200 corresponded to that of a RCCA/RMIC, as was the case for the NT1.1–AC.

The presence of the Laves phase that was suggested by the XRD data was not confirmed by a detailed study of the microstructure using EDS. In other words, both the Laves phase and the eutectic that were observed in NT1.1–AC were not stable after the two heat treatments. The typical microstructure of NT1.1–HT200 is shown in Figure 18, which shows that Ti-rich silicide also formed (Table 3) in between $A15–Nb_3X$ grains. The volume fraction of the Ti-rich silicide was low (Table 2). In Tables 2 and 3, the data of NT1.1–HT200 are for the bulk, i.e., for phases uncontaminated with oxygen.
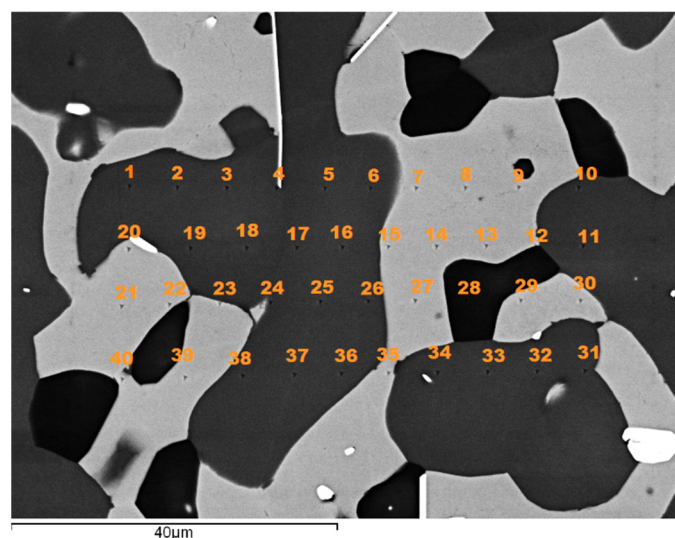
Figure 18. Back scatter electron image of the microstructure of NT1.1–HT200. Dark phase: βNb_5Si_3, very dark phase: Ti-rich silicide, grey phase: $A15–Nb_3X$, bright phase: hafnia. The numbers correspond to nanoindentation points.

Table 3. Chemical composition (at.%, average and standard deviation value) of phases in NT1.1–HT200.

Phase	Nb	Ti	Si	Al	Cr	Hf	Mo	W	Sn	Ge
βNb_5Si_3	36.3 ± 0.9	20 ± 1.0	21.9 ± 0.4	4.6 ± 0.2	3.3 ± 0.1	0.45 ± 0.2	3.6 ± 0.2		3.4 ± 0.4	6.3 ± 0.2
Ti-rich Nb_5Si_3	31.2 ± 0.3	24.8 ± 0.3	24.4 ± 0.3	5.1 ± 0.1	3.1 ± 0.1	0.8 ± 0.4	2.9 ± 0.1		1.0 ± 0.1	6.9 ± 0.1
A15-Nb_3X	39.3 ± 0.4	17.6 ± 0.2	4.2 ± 1.3	6.8 ± 0.2	7.7 ± 0.7		11.7 ± 0.6	1.9 ± 0.1	8.8 ± 0.2	1.9 ± 0.3

The βNb_5Si_3 silicide (Nb/(Ti + Hf) = 1.77), Ti-rich silicide (Nb/(Ti + Hf) = 1.22) and the A15–Nb_3X compound were the stable phases in NT1.1–HT. Similarly with NT1.2–HT, Ti-rich silicide was formed but instead of the bcc (A2) solid solution that was stable in the alloy NT1.2, the A15–Nb_3X was stable in the alloy NT1.1. The stable intermetallics in NT1.1 were "complex concentrated" (CC, or "compositionally complex"), as was the case with the silicides in NT1.2 [46]. The Nb/(Ti + Hf) ratios of the silicide corresponded to those of tetragonal Nb_5Si_3 [51], in agreement with the XRD data. No Ti-rich A15–Nb_3X was observed in NT1.1–HT after both heat treatments.

Compared with the βNb_5Si_3 in NT1.1–AC (Table 1), the βNb_5Si_3 in NT1.1–HT200 was richer in Al, Cr, Ge, Sn and Ti and poorer in Hf, Mo, Nb, Si and W (Table 3) and the Ti-rich silicide was richer in Al, Cr, Ge and Ti and poorer in Hf, Mo, Nb, Si, Sn and W. Essentially, the silicide was W-free. Compared with the A15–Nb_3X in NT1.1–AC (Table 1), there were notable changes in the concentrations of Mo and Nb, that, respectively, decreased and increased, as well as a decrease in the Ti content of the A15–Nb_3X in NT1.1–HT200 (Table 3). Below, we shall consider each phase separately.

Relationships between solutes in A15–Nb_3X are shown in Figure 19. The concentrations of Si and Ge increased with Ti content (Figure 19b,c), whereas those of Cr, Sn and Mo decreased (Figure 19a,d,h). With increasing Si concentration, the Ge content increased (Figure 19e) while those of Sn, Mo and W decreased (Figure 19f,k,l). With increasing Ge concentrations, the Sn and Mo contents decreased (Figure 19g,i) and that of Ti increased (Figure 19c). Correlations of solutes with Al were less strong ($R^2 < 0.7$). The Al concentration in the A15–Nb_3X decreased as its Ge, Si and Ti concentrations increased, whereas it increased with increasing Mo and Sn concentrations.

Figure 19a,b,e,f,h,k,l gives for the first time new data for the A15–Nb_3X, and Figure 19c,i is in agreement with data for NT1.1–AC (Figure 11e,j). However, the trends shown in Figure 19d,g,j are opposite those in NT1.1–AC (Figure 11i,g), owing to changes in the chemical composition of phases that occurred after the heat treatment and the absence of the Laves phase and the eutectic in NT1.1–HT.

(a)

(b)
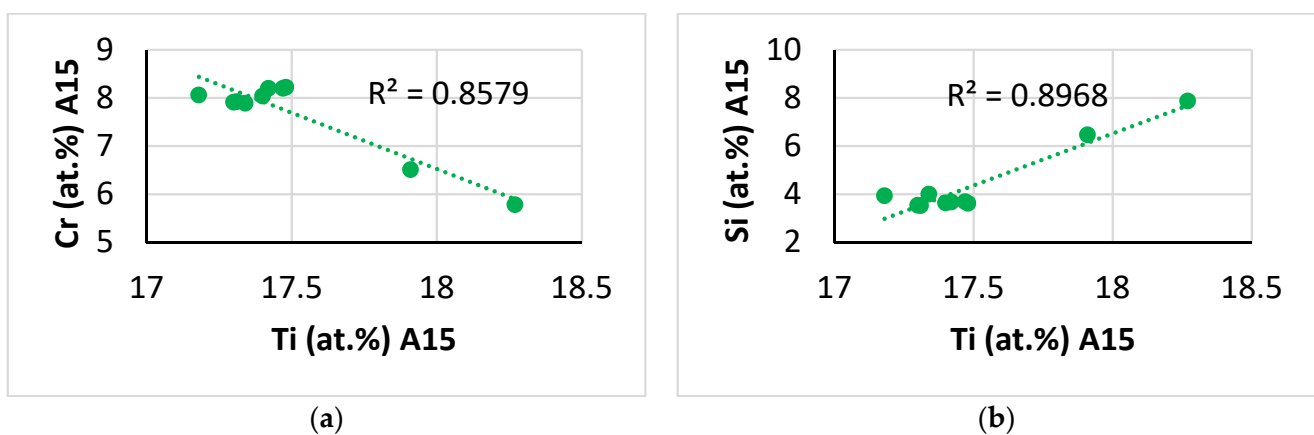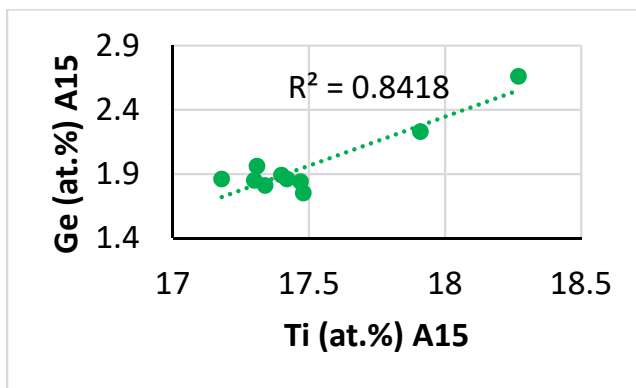
Figure 19. *Cont.*

(c)
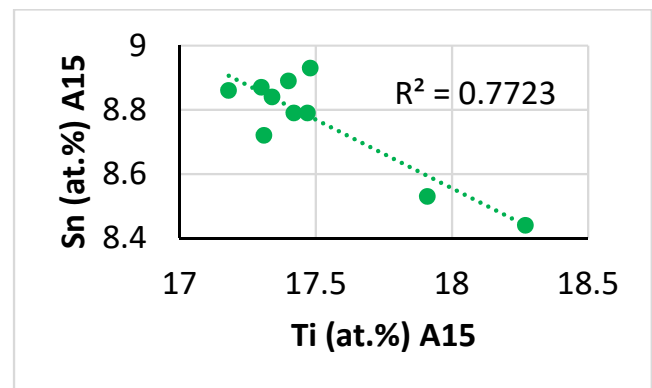
(d)
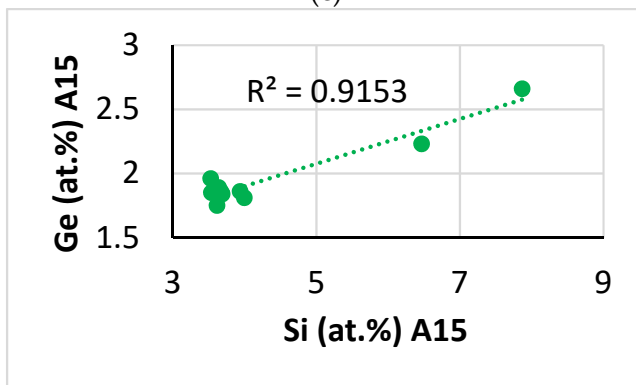
(e)
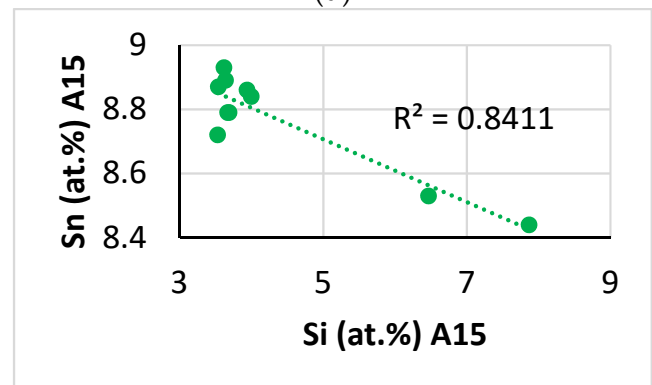
(f)
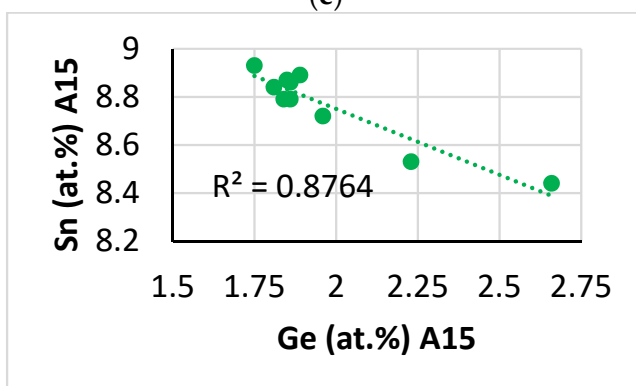
(g)

(h)

(i)

(j)

Figure 19. *Cont.*

(**k**)

(**l**)
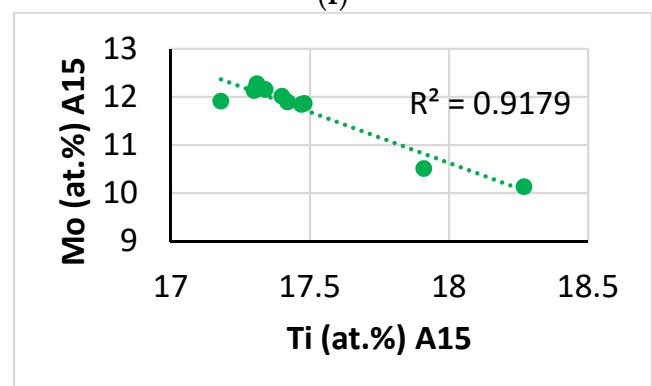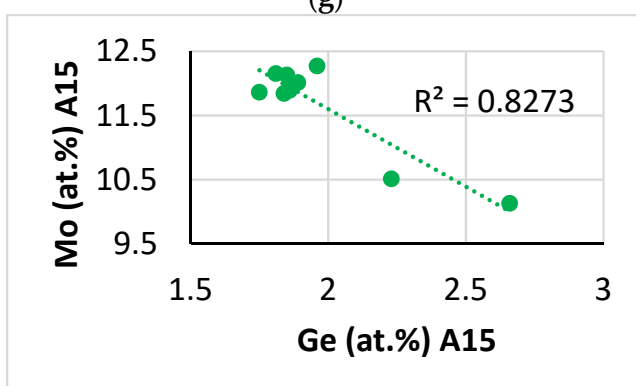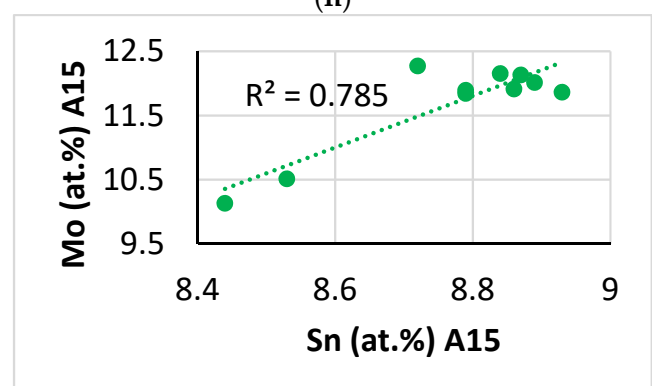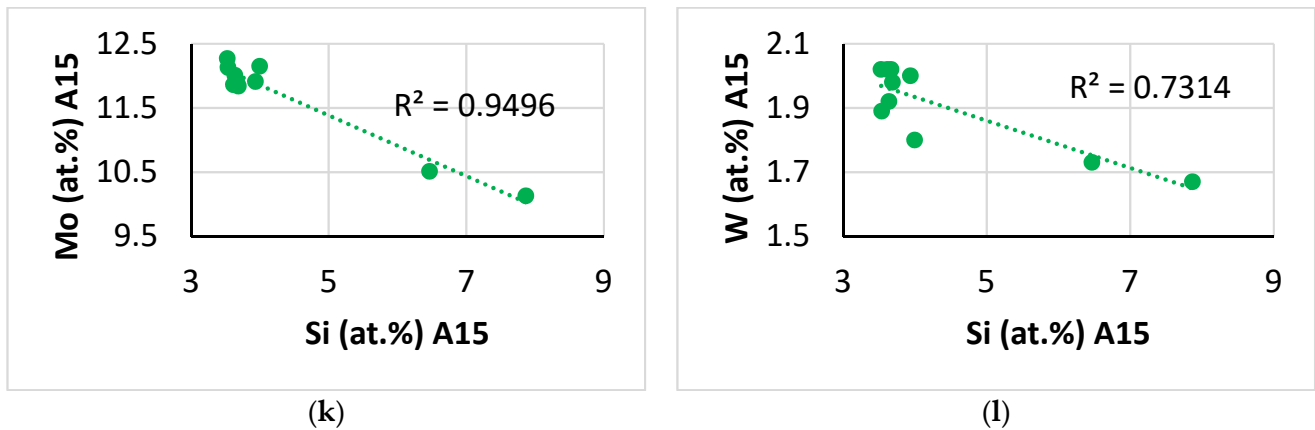
Figure 19. Relationships between solutes in A15-Nb$_3$X (X = Al, Ge, Si, Sn) in NT1.1–HT200. (**a**) Cr versus Ti, (**b**) Si vs. Ti, (**c**) Ge vs. Ti, (**d**) Sn vs. Ti, (**e**) Ge vs. Si, (**f**) Sn vs. Si, (**g**) Sn vs. Ge, (**h**) Mo vs. Ti, (**i**) Mo vs. Ge, (**j**) Mo vs. Sn, (**k**) Mo vs. Si, (**l**) W vs. Si.

Relationships between the parameters VEC, Δχ and solutes in A15–Nb$_3$X in NT1.1–HT are shown in Figure 20. Both the Δχ and VEC parameters increased with Mo content (Figure 20a,b), as was the case in NT1.1–AC (Figures 12b and 13b), and decreased with increasing <X> = Al + Ge + Si + Sn concentration (Figure 20c,d). Figure 20c,d gives for the first time new data about relationships of the parameters Δχ and VEC with <X> of A15–Nb$_3$X. The parameter VEC increased with increasing Δχ (Figure 20e), the same trend as in NT1.1–AC (Figure 14).

(**a**)

(**b**)

(**c**)

(**d**)

Figure 20. *Cont*.

(**e**)
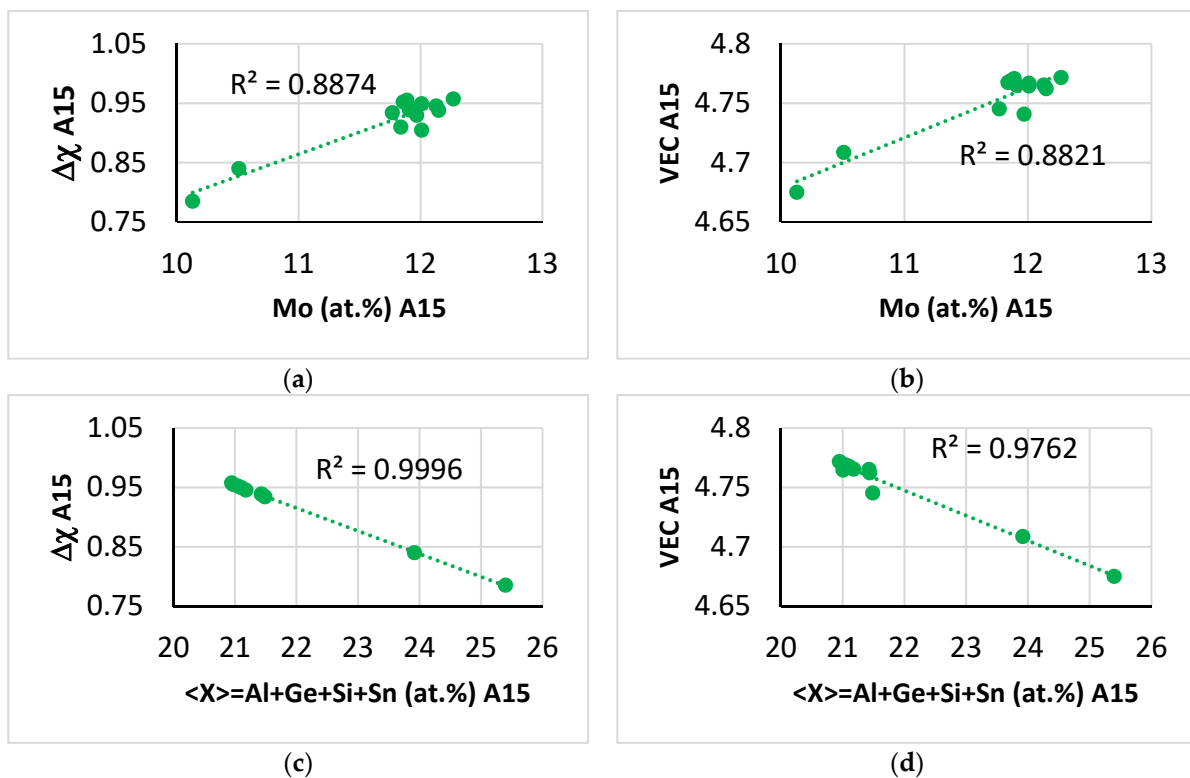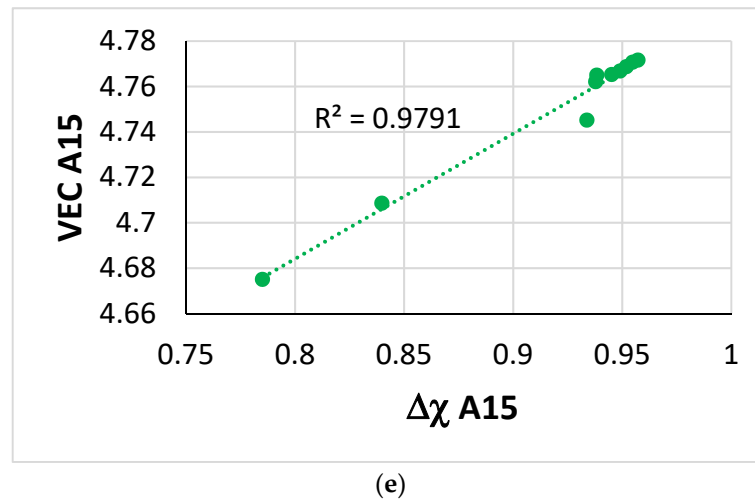
Figure 20. Relationships between the parameters VEC, $\Delta\chi$ and solutes in A15–Nb$_3$X in NT1.1–HT. (**a**) $\Delta\chi$ versus Mo, (**b**) VEC vs. Mo, (**c**) $\Delta\chi$ vs. <X>, (**d**) VEC vs. <X>, (**e**) VEC vs. $\Delta\chi$ map. <X> = Al + Ge + Si + Sn.

Relationships between solutes in the silicide in NT1.1–HT are shown in Figure 21. Increasing the Al concentration in the silicide increased the concentrations of Ti, Si and Ge (Figure 21a,d,f) and decreased the concentrations of Mo, Cr and Sn (Figure 21b,c,e,l). An increase in the Ge content of the silicide decreased its Cr, Mo and Sn concentrations (Figure 21g–i) and increased the concentration of Si (Figure 21j), and the latter increase was accompanied by an increase in the Sn content (Figure 21k). Figure 21b,d–f,h–k gives for the first time new data for the Nb$_5$Si$_3$ and Figure 21a shows the same trend as Figure 7d. However, Figure 21c,g,l shows opposite trends compared with Figure 7g,f,e, owing to the changes in the chemical composition of phases that occurred after the heat treatment and the absence of the Laves phase and eutectic.

(**a**)

(**b**)

(**c**)

(**d**)
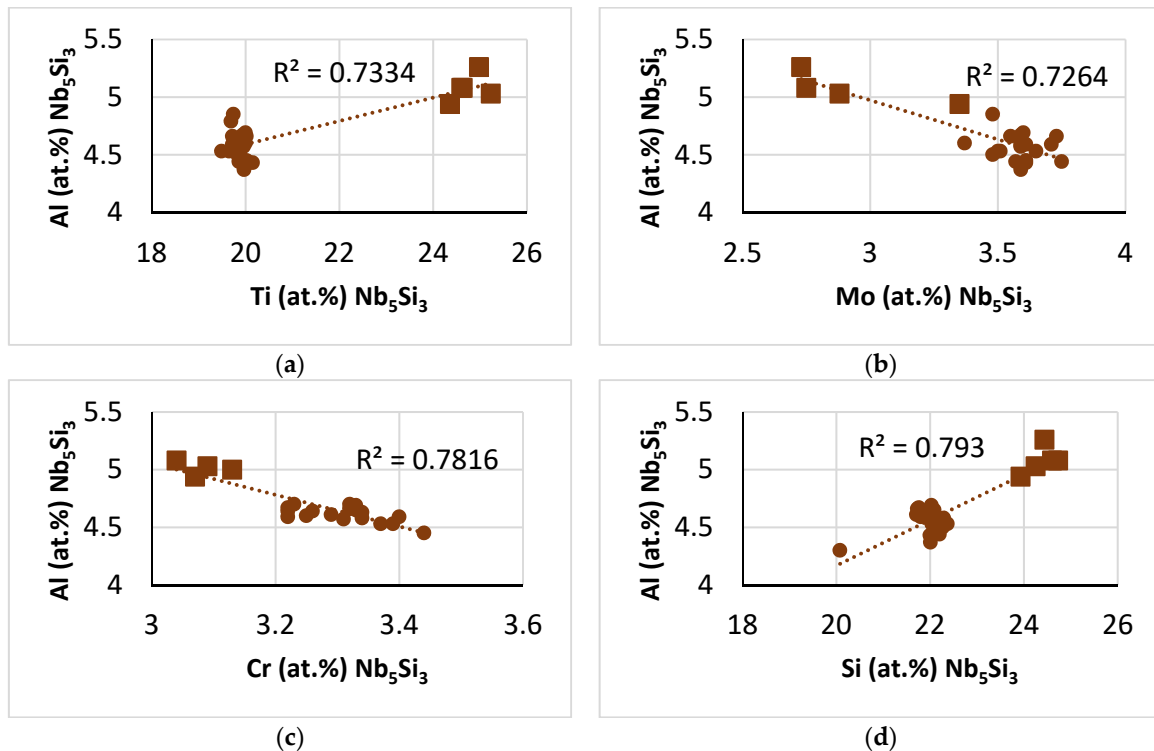
Figure 21. *Cont.*
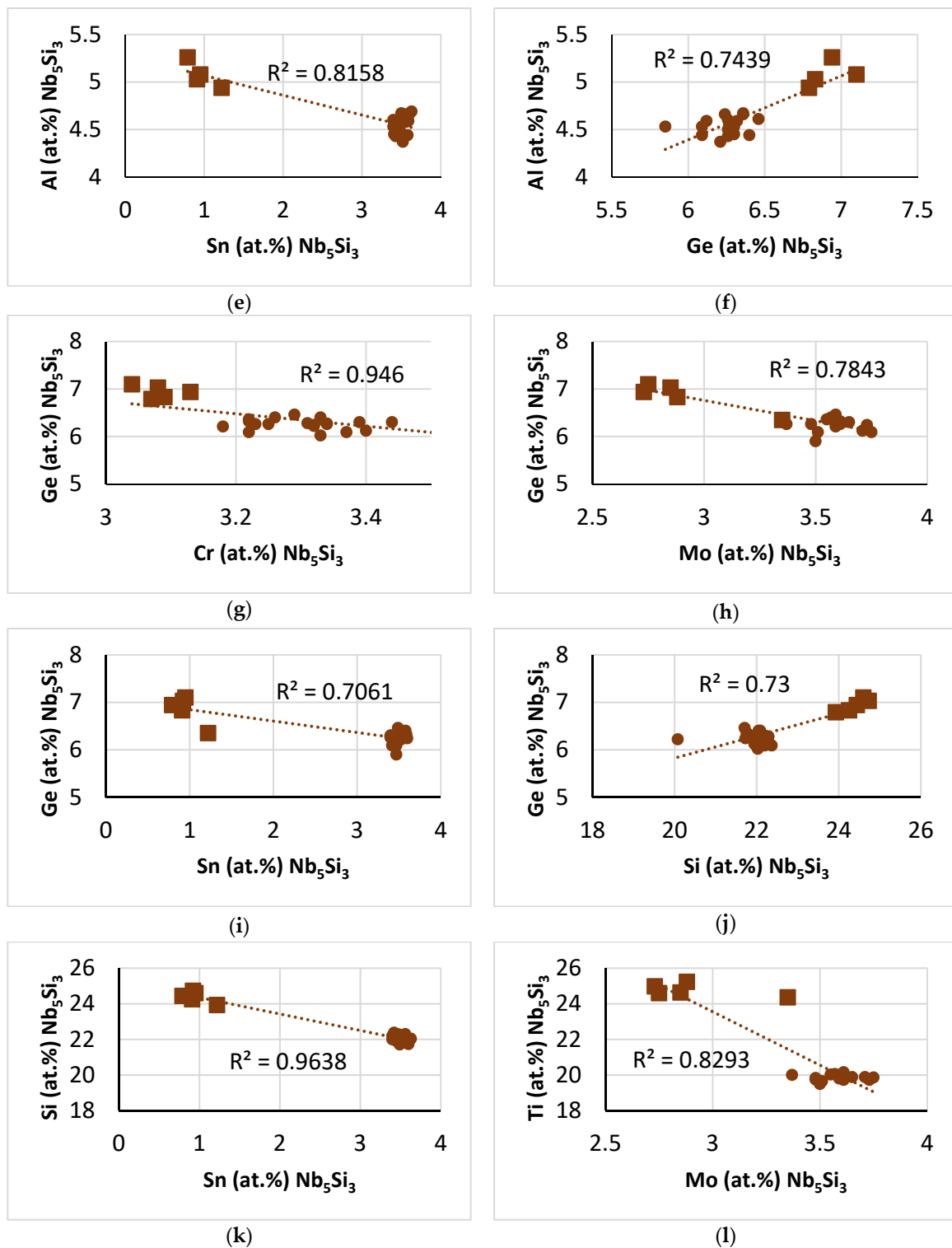
Figure 21. Relationships between solutes in βNb₅Si₃ in NT1.1–HT. Squares for Ti-rich silicide. (**a**) Al versus Ti, (**b**) Al vs. Mo, (**c**) Al vs. Cr, (**d**) Al vs. Si, (**e**) Al vs. Sn, (**f**) Al vs. Ge, (**g**) Ge vs. Cr, (**h**) Ge vs. Mo, (**i**) Ge vs. Sn, (**j**) Ge vs. Si, (**k**) Si vs. Sn, (**l**) Ti vs. Mo.

Relationships between the parameters VEC and Δχ and solutes in Nb₅Si₃ are shown in Figure 22. The parameter VEC decreased with increasing Ge and Ti concentrations in the silicide, in agreement with the data for NT1.1–AC (Figure 8), but not for the parameter Δχ, which also decreased with increasing Ge and Ti concentrations in the silicide (see Figure 9).

Compared with the Ti-rich silicide, the VEC of βNb_5Si_3 changed very little as the Ge content of the silicide increased (Figure 22b).
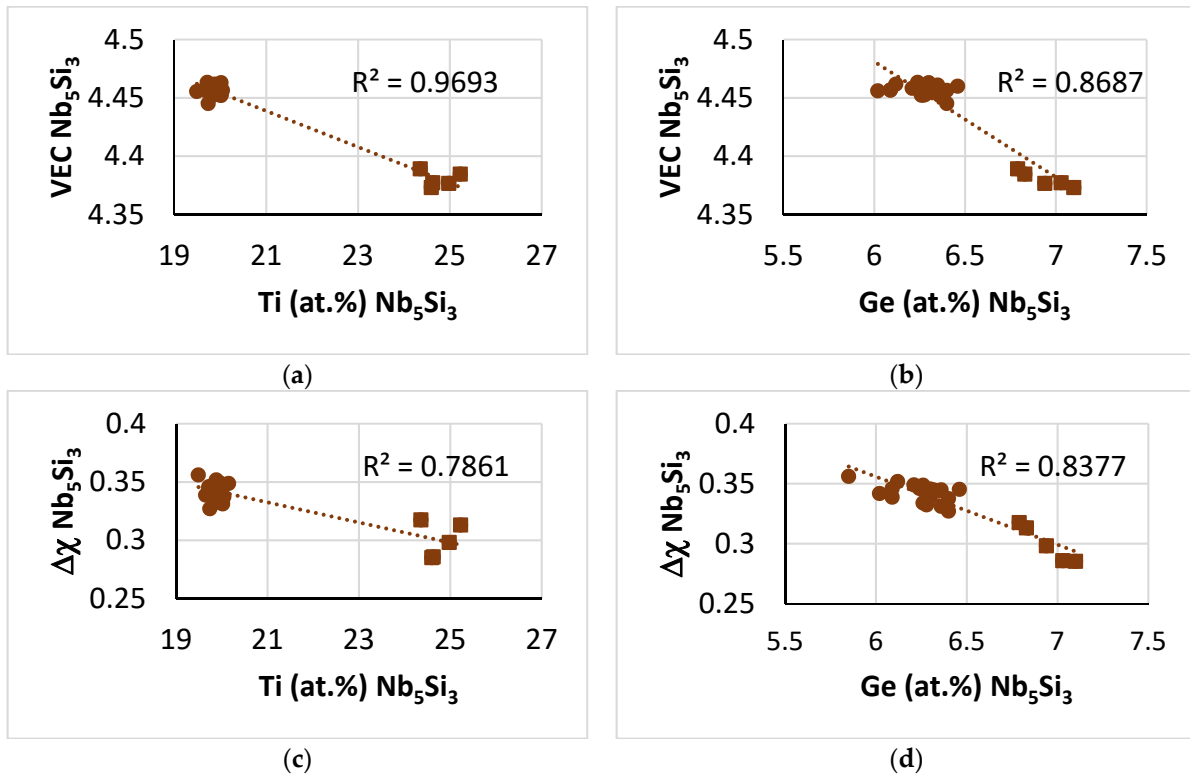
Figure 22. Relationships between the parameters VEC and $\Delta\chi$ and solutes in Nb_5Si_3 in NT1.1-HT. Squares for Ti-rich silicide. (**a**) VEC versus Ti, (**b**) VEC vs. Ge, (**c**) $\Delta\chi$ vs. Ti, (**d**) $\Delta\chi$ vs. Ge.

VEC versus $\Delta\chi$ maps of the βNb_5Si_3 are shown in Figure 23. Figure 23b, which includes data for the binary (unalloyed) βNb_5Si_3, should be compared with the data for the B-free silicide in Figure 6 in [60]. The comparison shows that the same trend was followed for the silicide in NT1.1–HT, as was the case for NT1.1–AC (Figure 10b). However, owing to the changes in the chemical composition of the βNb_5Si_3 after heat treatment, the trend in the VEC versus $\Delta\chi$ map of the βNb_5Si_3, excluding data for the unalloyed Nb_5Si_3, which is shown in Figure 23a, was opposite that shown in Figure 10a for the βNb_5Si_3 in NT1.1–AC.
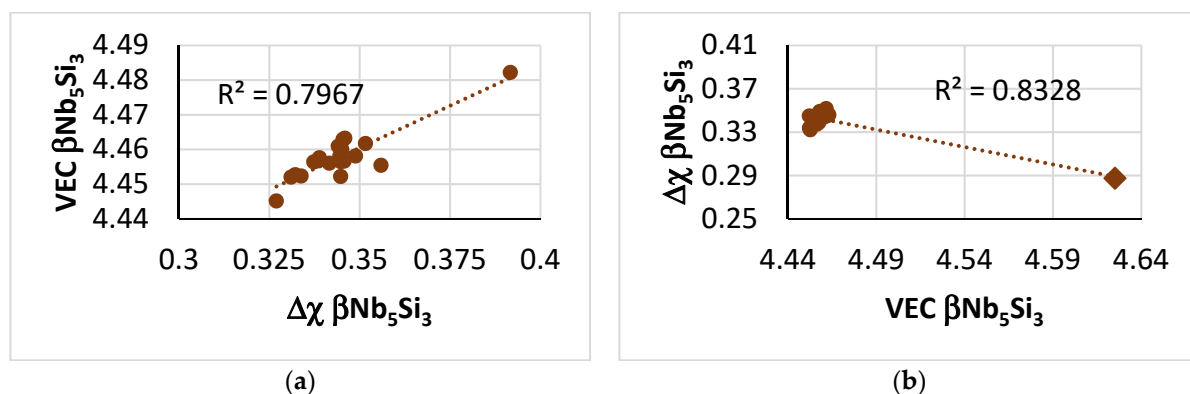
Figure 23. Maps of the parameters VEC and $\Delta\chi$ of the alloyed βNb_5Si_3 in NT1.1–HT. (**a**) VEC versus $\Delta\chi$, (**b**) $\Delta\chi$ vs. VEC with data (diamond) for the binary (unalloyed) βNb_5Si_3.

The VEC versus $\Delta\chi$ map of the stable phases in NT1.1–HT is shown in Figure 24a. The map shown in Figure 16 "evolved" to that in Figure 24a after the heat treatment. We

can show the "evolution" of microstructure at a particular temperature using a VEC, Δχ, time diagram (see Figure 24b). The latter is specific to T = 1500 °C, and shows (i) that the silicide "evolved" to Ti-rich silicide and βNb₅Si₃, (ii) that the Laves phase and eutectic were not stable and (iii) that the A15–Nb₃X high <X> also was not stable. To the authors' knowledge, this is the first time that the "evolution" of microstructure is shown for a RCCA/RMIC using VEC versus Δχ maps and a VEC, Δχ, time diagram. This "evolution" links the metallic UHTM with risk (IRIS) and environment–material interactions (CEMI) and enhances the capabilities of "synergistic" metallurgy regarding alloy development; see Section 7 in [12] and Section 4 below.

The nano-hardness and Young's modulus of the stable phases in NT1.1–HT were studied using nanoindentation. EDS was used to determine the chemical composition of each phase as close as possible to the nanoindentation points. In nanoindentation, from the unloading curve the stiffness, S, the phase can be measured. The stiffness is correlated with the reduced modulus E_r with the following equation:

$$S = \frac{dP}{dh} = \frac{2}{\sqrt{\pi}} E_r \sqrt{A}$$

where P is the load, h is the displacement and A is the projected surface area of the indentation. The reduced modulus E_r accounts for the effects of a non-rigid indenter during loading and is given by the following equation:

$$\frac{1}{E_r} = \frac{(1 - \nu_s^2)}{E_s} + \frac{(1 - \nu_i^2)}{E_i}$$

where E_s and ν_s are Young's modulus and Poisson's ratio of the phase and E_i, ν_i are the parameters for the indenter [65]. A rearrangement of the last equation gives the actual modulus, E_s, of the phase as follows:

$$E_s = \frac{E_r E_i (1 - \nu_s^2)}{E_i - E_r (1 - \nu_i^2)}$$

The values of E_i and ν_i were specified in the TriboScope manual [66] as 1140 GPa and 0.07, respectively. The E_s was calculated for two different values of ν_s, namely 0.320 for the A15–Nb₃X (the average of the Poisson ratio values for A15 Nb₃Al, Nb₃Ge, Nb₃Si, Nb₃Sn [67]), and 0.263 for the silicide [68].

The nano-hardness and Young's modulus data for the microstructure in Figure 18 are shown in Figure 25. The average Young's modulus and nano-hardness values, respectively, for the two phases in NT1.1–HT200 were E_s = 232.6 ± 5.4 GPa (range of 219.4 to 244.8 GPa), nanoH = 17.2 ± 0.5 GPa (range of 16.5 to 18.1 GPA) for the βNb₅Si₃, and E_s = 204.5 ± 7.3 GPa (range of 181.2 to 217 GPa), nanoH = 14.7 ± 0.4 GPa (range of 13.4 to 15.3 GPa) for the A15–Nb₃X. The Ti-rich silicide had E_s = 258.7 GPa and nanoH = 20.5 GPa. In NT1.1–HT200, the difference in the properties of the βNb₅Si₃ and the Ti-rich silicide was significant. Compared with the data for the alloy NT1.2 [46], Young's modulus of the βNb₅Si₃ was slightly lower and the nano-hardness was essentially the same (E_s = 250.3 GPa, nanoH = 17.6 GPa), but for the Ti-rich silicide, Young's modulus was significantly lower (E_s = 281.5 GPa) and the nano-hardness slightly lower (nanoH = 19.2 GPa). Young's modulus of the Ti-rich silicide in NT1.1–HT200 was very similar to that of the βNb₅Si₃ in NT1.2. (Note that the Ti-rich silicide in NT1.1 was richer in Al and Cr and poorer in Si and Ti compared with the Ti-rich silicide in NT1.2, with Nb/(Ti + Hf) ratios, respectively, 1.21 and 1.13.)

(a)

(b)
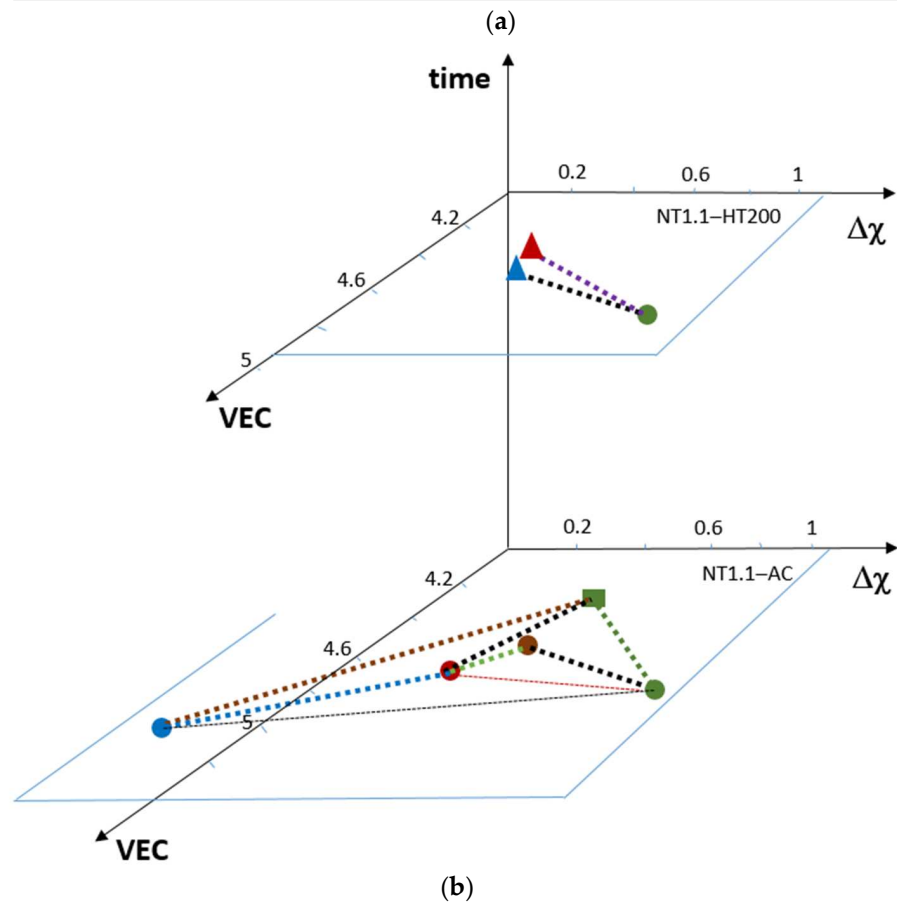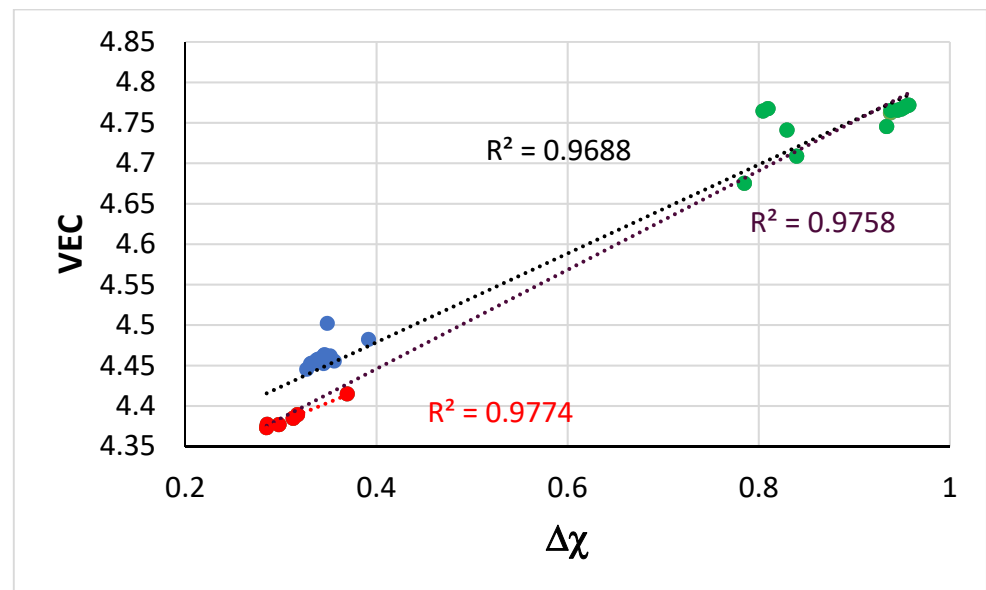
Figure 24. (**a**) VEC versus $\Delta\chi$ map of the phases in NT1.1–HT200. Data are shown with filled circles. Colours as follows: green, A15–Nb$_3$X; blue, βNb$_5$Si$_3$; red, Ti-rich silicide. Correlations as follows: R^2 = 0.9774 data for Ti-rich silicide, R^2 = 0.9758 data for A15–Nb$_3$X and Ti-rich silicide, R^2 = 0.9688 data for A15–Nb$_3$X and βNb$_5$Si$_3$. (**b**) VEC, $\Delta\chi$, time diagram showing "evolution" of microstructure at T = 1500 °C. See Figure 16 for the NT1.1–AC. For the VEC versus $\Delta\chi$ map of the as-cast alloy, the colours are as follows: blue for C14–NbCr$_2$-based Laves phase, red for eutectic, brown for βNb$_5$Si$_3$, green for A15–Nb$_3$X. Square for A15–Nb$_3$X with high <X>. For the VEC versus $\Delta\chi$ map of the heat-treated alloy, the triangles correspond to the silicide and the colours are as follows: green for A15–Nb$_3$X, red for Ti-rich silicide and blue for βNb$_5$Si$_3$.

(**a**)

(**b**)
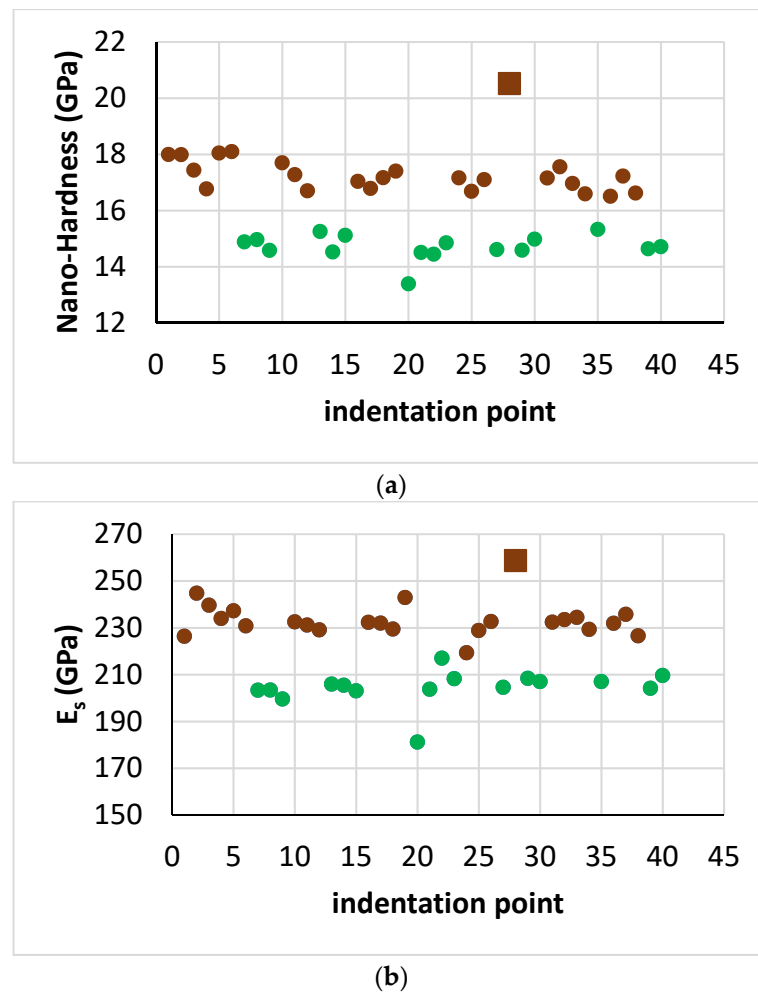
Figure 25. (**a**) Nano-hardness and (**b**) Young's modulus data for the microstructure shown in Figure 18. Colours as follows: brown—βNb_5Si_3, green—A15 Nb_3X, square for Ti-rich silicide (indentation point 28 in Figure 18).

In the nano-hardness data of the βNb_5Si_3, note the repeated downward trends in nano-hardness (i.e., decrease in nano-hardness) between the nanoindentation points 2, 3, 4 and 10, 11, 12 and 16, 17 and 24, 25 and 32, 33, 34 and 37, 38 and the repeated upward trends in nano-hardness (i.e., increase in nano-hardness) between the nanoindentation points 17, 18, 19 and 25, 26 and 31, 32 and 36, 37 (Figure 25a). In Young's modulus data of the βNb_5Si_3, note the repeated downward trends of E_s (i.e., decrease in E_s) between the nanoindentation points 2, 3, 4 and 5, 6 and 37, 38, and between the points 10, 11, 12 and 16, 17, 18, and the upward trends of E_s (i.e., increase in E_s) between the nanoindentation points 1, 2 and 18, 19 and 24, 25, 26 (Figure 25b). Similarly, the nano-hardness of A15–Nb_3X increased between nanoindentation points 20, 21, 22, 23 (Figure 25a) and Young's modulus between nanoindentation points 20, 21, 22 (Figure 25b). The property changes in specific areas of the microstructure shown in Figure 18 were associated with changes in the parameters VEC and $\Delta\chi$ (Figure 26).

(a)

(b)
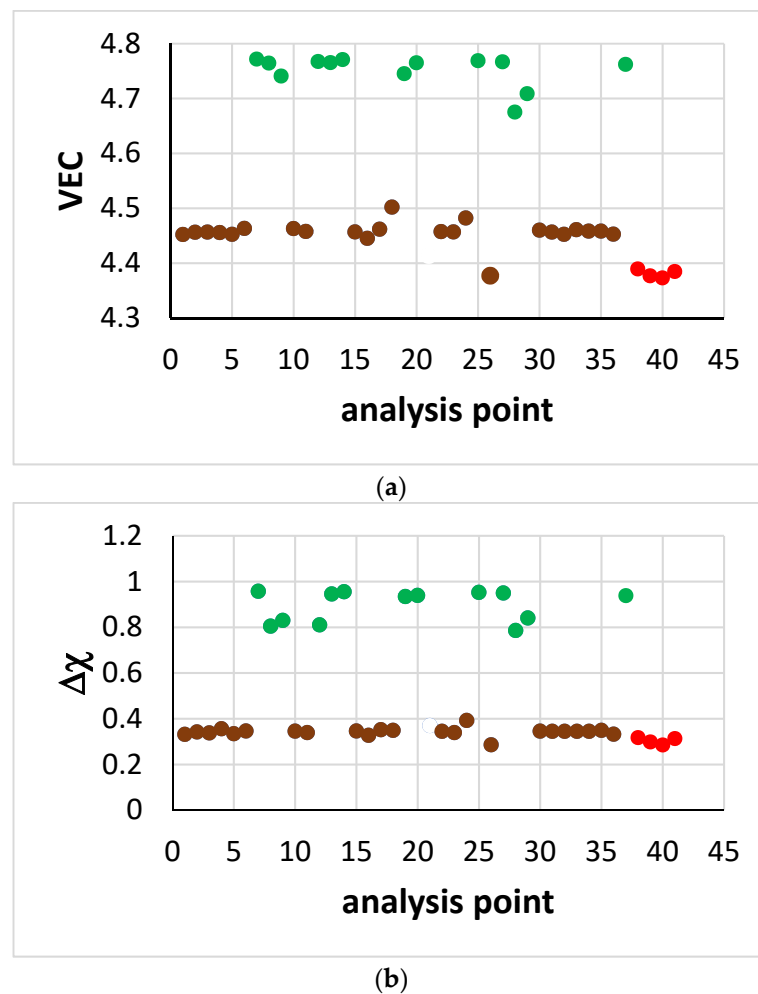
Figure 26. The parameters VEC (**a**) and $\Delta\chi$ (**b**) of the microstructure shown in Figure 18. The analysis point numbers correspond as closely as possible to the nanoindentations. Colours as follows: brown, βNb_5Si_3; green, A15–Nb_3X; red, Ti-rich silicide (very dark contrast grains above points 7, 8, near 28, between 39 and 40 and below 40 in Figure 18).

The parameters VEC and $\Delta\chi$ of the microstructure in Figure 18 are shown in Figure 26. The parameter $\Delta\chi$ of the silicide exhibited less variation between points compared with the parameter VEC, and the opposite was the case for the parameters of the A15–Nb_3X. Whereas between the nanoindentation points 1 to 6 the change in the VEC parameter of βNb_5Si_3 was marginal, between the nanoindentation points 16, 17 and 18, a change in VEC was clear (Figure 26a). Similarly, whereas there was a marginal change in the parameter VEC of the A15–Nb_3X between the nanoindentations 12, 13 and 14, and a slight change between the nanoindentations 7, 8 and 9, a change in $\Delta\chi$ was noticeable between the said nanoindentation points (Figure 26b). The $\Delta\chi$ parameter of the Ti-rich silicide (red data in Figure 26b) did not differ significantly from that of the βNb_5Si_3 but its VEC was noticeably lower (Figure 26a).

In the alloy NT1.1–HT, the silicide was the $\beta(Nb,Cr,Hf,Mo,Ti,W)_5(Al,Ge,Si,Sn)_3$, the Nb was substituted by Cr, Hf, Mo, Ti and W, and the Si was substituted by Al, Ge and Sn. The A15 compound was the A15–$(Nb,Cr,Hf,Mo,Ti,W)_3(Al,Ge,Si,Sn)$, the Nb was substituted by Cr, Hf, Mo, Ti and W, and the Si was substituted by Al, Ge and Sn. The calculated Young's modulus of binary (unalloyed) Nb_5Si_3 is 291, 268.9 and 188.5 GPa for the αNb_5Si_3, βNb_5Si_3 and γNb_5Si_3 polymorphs, respectively [68]. Also, for the αNb_5Si_3 polymorph, Young's moduli of 314.3 and 325 GPa have been reported, respectively, in [69,70]. The data in [68] show that for 12.5 at.% Ti addition in the silicide the calculated Young's moduli of

α(Nb,Ti)$_5$Si$_3$, β(Nb,Ti)$_5$Si$_3$ and γ(Nb,Ti)$_5$Si$_{3, \text{respectively}}$, were 313.8, 238.5 and 207.1 GPa. In other words, according to first-principles calculations, the substitution of Nb by Ti in the silicide increased the modulus of the α and γ polymorphs and decreased the modulus of the β polymorph.

The calculated Young's moduli of A15 Nb$_3$Al, Nb$_3$Ge, Nb$_3$Si and Nb$_3$Sn, respectively, are 164, 193.3, 210 and 172.7 GPa [67]. For the A15 Nb$_3$Al and Nb$_3$Sn, the values of 193.5 and 195.3 GPa, respectively, were also reported in [71] and the experimental modulus of 179 GPa was reported by Old and Charlesworth [72,73]. As the A15–Nb$_3$X was rich in Mo, we also considered data for A15–Mo$_3$X compounds. The calculated Young's moduli of A15 Mo$_3$Al and Mo$_3$Ge were 312.3 GPa and 315.7 GPa, respectively [74,75]. For A15 Mo$_3$Si, calculated Young's moduli were 338.3 GPa [75], 315.9 GPa [76], 370 GPa [77] and 343 GPa [78] and experimental moduli were 327.5 GPa [79] and 295 GPa [80]. The calculated modulus of 333 GPa of Mo$_3$Si increased when alloyed with 12 at.% addition of Al or Nb, respectively, to 347 GPa and 344 GPa [81]. For thin films of Nb$_3$Sn deposited on Nb substrates, the experimental Young's modulus of Nb$_3$Sn was in the range of 150.1 to 201.9 GPa [82]. A low Young's modulus of 134.9 GPa has also been reported for Nb$_3$Sn [83].

The Young's modulus and hardness of the alloyed βNb$_5$Si$_3$ in NT1.1–HT200 were close to the properties of the β(Nb,Cr,Hf,Ti)$_5$(Al,Si)$_3$ silicide in the RMIC alloy JN1-HT (241.4 GPa and 17.4 GPa, respectively) [84]. Our group reported that the substitution of Si by Ge in the silicide increases the hardness of the latter [61]. This was supported by the recent work of Zhaobo Li et al. [85], who reported that the nano-hardness and Young's modulus of the β(Nb,Cr,Ti)$_5$(Al,Ge,Si)$_3$ silicide in the as-cast RM(Nb)IC (Nb silicide-based alloy) Nb–22Ti–16Si–2Al–2Cr–5Ge was 21.46 GPa and 279.2 GPa, respectively.

The Young's modulus of the alloyed βNb$_5$Si$_3$ in NT1.1–HT200 was close to that of the β(Nb,Ti)$_5$Si$_3$ (see above) and that of the Ti-rich silicide was close to that of unalloyed β(Nb,Ti)$_5$Si$_3$. It is suggested that the Ti-rich silicide in NT1.1–HT was Ti-rich β(Nb,Ti)$_5$Si$_3$. The Young's modulus of the alloyed A15–Nb$_3$X was significantly lower than that of unalloyed Mo$_3$X compounds (X = Al, Ge, Si) and close to that of A15–Nb$_3$X compounds (X = Al, Ge, Si, Sn). In actual fact, Young's modulus of the alloyed A15–Nb$_3$X was very close to that of the A15–Nb$_3$Si and the γ(Nb,Ti)$_5$Si$_3$.

To the authors' knowledge, nano-hardness data for binary or alloyed A15 compounds are not available in the open literature. We have calculated the hardness of binary (unalloyed) A15–M$_3$X (M = Mo, Nb and X = Al, Ge, Si, Sn) compounds using the following equations [86]:

$$HV_1 \text{ (GPa)} = [(1 - 2\nu)E]/[6(1 + \nu)] \tag{1}$$

$$HV_2 \text{ (GPa)} = 2[(G/B)^2G]^{0.585} \tag{2}$$

$$HV_3 \text{ (GPa)} = 0.151\,G \tag{3}$$

with data for the bulk modulus B, shear modulus G, Young's modulus E and Poisson ratio ν from the literature. The calculated hardness data are given in Table 4.

Table 4. Calculated hardness of binary A15–M_3X (M = Mo, Nb and X = Al, Ge, Si, Sn) compounds using Equations (1)–(3) and property data from the literature.

Binary A15 Compound	Hardness (GPa)			Property Data From
	HV$_1$	HV$_2$	HV$_3$	
Nb$_3$Al	6.9	7.2	9.3	67
Nb$_3$Ge	9.1	9.0	11.1	67
Nb$_3$Si	10.3	10	12.1	67
Nb$_3$Sn	7.5	7.6	9.8	67
	5.1	5.5	7.8	83
Mo$_3$Al	18.9	16.0	18.3	74
Mo$_3$Ge	18.3	15.6	18.6	75
Mo$_3$Si	20.4	17.1	20.1	75
	19	16.4	18.8	76
	21.4	17.1	21.9	77
	20.7	17.2	20.4	78
	19.5	16.4	19.4	79

The average and the minimum and maximum (i.e., the range) values of the nano-hardness of the alloyed A15–Nb$_3$X of this work were close to HV$_3$ of A15–Nb$_3$Si and HV$_2$ of A15–Mo$_3$Ge. Note that the experimental data of Pudasaini et al. [82] for A15–Nb$_3$Sn thin films on Nb substrates showed that the thin film with the highest E (201.9 GPa) had nanoH = 12.8 GPa, whereas the film with nanoH = 14.4 GPa had E = 161.2 GPa.

The calculated HV$_1$ of the β(Nb,Cr,Hf,Mo,Ti,W)$_5$(Al,Ge,Si,Sn)$_3$ silicide of this work, using Equation (1) with the experimental Young's modulus (average, and range (minimum and maximum)) values given above and ν = 0.281 from [67] for βNb$_{16}$Ti$_4$Si$_{12}$, was 13.3, 12.5 and 14 GPa, respectively, for the average, minimum and maximum E$_s$ values. All three calculated values of nanoH were lower than the experimental ones.

If we were to use the experimental nanoindentation and chemical analysis data for the A15–Nb$_3$X and silicide grains in NT1.1–HT200 and calculate the change in a property or parameter per atomic percent addition of solute X (i.e., calculate $\Delta P/X$) using the maximum and minimum concentration values of X (i.e., C$_{\text{max.}}$ $_X$ and C$_{\text{min.}}$ $_X$, respectively) and the corresponding property or parameter values for the aforementioned concentrations, we obtain the data for the alloyed βNb$_5$Si$_3$ and A15–Nb$_3$X shown in Tables 5 and 6, respectively. In these tables, $\Delta P/X = (P_{\text{max.}}$ $_X - P_{\text{min.}}$ $_X)/(C_{\text{max.}}$ $_X - C_{\text{min.}}$ $_X)$, where P is (i) a property, namely Young's modulus or nano-hardness (shown as HV in Tables 5 and 6), or (ii) a parameter, namely VEC or $\Delta\chi$. This is the same approach to the calculation of property or parameter changes per at.% solute that was discussed in [46].

Table 5. Data for properties and parameters of the alloyed βNb$_5$Si$_3$ in NT1.2-HT200. Average change of E$_s$, nano-hardness, VEC and $\Delta\chi$ per change in concentration of solute X.

Solute X	$\Delta E_S/X$ (GPa/at.%)	$\Delta[HV]/X$ (GPa/at.%)	$\Delta[VEC]/X$	$\Delta[\Delta\chi]/X$
Al	−7.83	−0.91	−0.0271	−0.0457
Cr	−2.65	+1.78	+0.0137	−0.0202
Ge	−2.57	+0.63	+0.0075	−0.0178
Hf	+1.37	−0.92	−0.0074	+0.0104
Mo	+0.9	+0.4	+0.0476	+0.083
Nb	−1.39	+0.11	+0.0236	+0.0370

Table 5. *Cont.*

Solute X	ΔE_S/X (GPa/at.%)	$\Delta[HV]$/X (GPa/at.%)	$\Delta[VEC]$/X	$\Delta[\Delta\chi]$/X
Si	−1.66	−0.18	−0.011	−0.023
Sn	+2.44	−0.29	+0.04	+0.085
Ti	+8.77	+0.68	−0.002	−0.0182
W	+3.62	+2.28	−0.0065	+0.18

Table 6. Data for properties and parameters of the A15-Nb$_3$X in NT1.2-HT200. Average change of E$_s$, nano-hardness, VEC and $\Delta\chi$ per change in concentration of solute X.

Solute X	ΔE_S/X (GPa/at.%)	$\Delta[HV]$/X (GPa/at.%)	$\Delta[VEC]$/X	$\Delta[\Delta\chi]$/X
Al	−4.75	−1.76	+0.1	+0.22
Cr	−0.99	−0.06	+0.038	+0.07
Ge	+2.83	−0.29	−0.07	−0.015
Mo	−1.71	+0.14	+0.045	+0.08
Nb	−3.2	+0.91	−0.03	−0.08
Si	+0.74	+0.27	−0.016	−0.07
Sn	−6.35	+0.66	+0.157	+0.03
Ti	−9.2	+0.07	−0.08	−0.14
W	−10.84	+0.215	+0.272	+0.484

To understand the data in Tables 5 and 6, we must consider the microstructure of NT1.2–HT, relationships between solutes, between solutes and parameters, between parameters of specific phases and between phases. We shall make use of the above discussion, Figures 19–24, and the concepts of synergy and entanglement that were discussed in [46].

Consider the synergy and entanglement of A15–Nb$_3$X and βNb$_5$Si$_3$ (Figure 24). As Ge partitioned to the A15 and the silicide, the concentrations of Ti and Si increased (Figure 19c,e) and those of Sn and Mo decreased (Figure 19g,i) in the former intermetallic, and the contents of Al and Si increased (Figure 21f,j) and those of Cr, Mo, Sn and Si decreased (Figure 21g–j) in the latter intermetallic. The increase in Ti concentration in the A15–Nb$_3$X was accompanied by the decrease in its Cr content (Figure 19a), whereas in the βNb$_5$Si$_3$ the increase in Al content was accompanied by the increase in the Ti, Si and Ge concentrations (Figure 21a,d,f) and the decrease in the Mo, Cr and Sn concentrations (Figure 21b,c,e). Owing to changes in solute concentrations, the parameters $\Delta\chi$ and VEC of the A15–Nb$_3$X changed with Mo and <X> contents (Figure 20) and those of the βNb$_5$Si$_3$ changed with Ge and Ti content (Figure 22), and the alloyed silicide "shifted further away" from the unalloyed βNb$_5$Si$_3$ in the $\Delta\chi$ versus VEC map (Figure 23a).

Owing to synergy and entanglement, a change in the concentration of solute element X brought changes to properties and parameters of the βNb$_5$Si$_3$ silicide, namely the changes ΔE_S/X, $\Delta[\text{nano-H}]$/X (shown as $\Delta[HV]$/X in Tables 5 and 6), $\Delta[VEC]$/X and $\Delta[\Delta\chi]$/X (see Table 5). The same was the case for the A15–Nb$_3$X. Comparison with the data for ΔE_S/X, $\Delta[HV]$/X, $\Delta[VEC]$/X and $\Delta[\Delta\chi]$/X in Table 12 in [46] shows differences in the contributions of all elements, as well as differences in the sign (meaning positive or negative) of changes attributed to Cr, Hf, Mo, Si and Sn for ΔE_S/X, or Cr, Si, Sn and Ti for $\Delta[HV]$/X, or Al, Ge, Nb, Sn, Ti and W for $\Delta[VEC]$/X, or Al, Cr. Nb, Ti and W for $\Delta[\Delta\chi]$/X. For example, we note that for Ti in the β(Nb,Cr,Hf,Mo,Ti,W)$_5$(Al,Ge,Si,Sn)$_3$ silicide in NT1.1, the ΔE_s/Ti was positive and equal to +8.77 GPa/at.% compared with +6.28 GPa/at.% for the alloyed silicide in NT1.2 (see Table 12 in [46]), whereas it was negative (−2.432 GPa/at.%) for the β(Nb,Ti)$_5$Si$_3$ (see discussion of properties of alloyed silicide in Section 4.2 in [46]). Also, we note that for Al in the silicide, the ΔE_s/Al was negative (−1.24 GPa/at.%) in NT1.2 (Table 12 in [46]) and negative (−7.83 GPa/at.%) in NT1.1 (Table 5). These differences are

attributed to the βNb_5Si_3 being in synergy with $A15–Nb_3X$ in the alloy NT1.1 and not with the bcc (A2) solid solution, as was the case in the alloy NT1.2 [46].

Note that Table 6 shows for the first time how properties of $A15–Nb_3X$ in a RCCA/RMIC change with solute addition.

4. Comments about the Design, Development and Processing of Metallic UHTMs

Our research group has shown that taking into consideration the Pauling electronegativity or atomic size or VEC, (a) the "popular" cubic and hexagonal solutes in metallic UHTMs (see Section 1, and [7,60,62,64]) fall in specific groups regarding (i) elastic properties (see Figures 1–3a and 8 in [62], and Figure 1 in [60]); (ii) mass change in oxidation (see Figure 13 in [62]); (iii) creep (see Figure 14 in [61]); and (iv) diffusivities (see Figures 1–4 in [87]), and (b) the elastic properties of desirable $A15–Nb_3X$ compounds, tetragonal $D8_m$ silicides (tP32, prototype W_5Si_3) and tetragonal $D8_l$ (tP32, prototype Cr_5B_3) silicides (see Section 1), and [7,60,62,64]) exhibit specific trends (see, respectively, Figures 3d and 4a, Figures 3b and 4b, and Figures 3c, 4c and 4d in [62]).

Our research group also has shown (c) relationships between the solutes that substitute (v) Nb or Cr in the $C14–NbCr_2$ Laves phase and its parameters VEC, $\Delta\chi$ and atomic size (see Figures 1–3 in [44]) and (vi) Nb or Si in Nb_5Si_3, see Figures 5–11 and Table 2 in [61] and Figure 6 in [60]). Owing to (i) to (vi) and synergy and entanglement [12], metallic UHTMs occupy specific positions in parameter maps when their oxidation and mechanical properties are considered (see Figure 1 in [63], Figure 19 in [7] and Figures 1 and 2 in [64]). The (a) and (b) form part of the substructure supporting the superstructure in the "alloy design landscape" of NICE (see Figure 1 in [12]) and guide the selection of alloying elements in alloy design, which in NICE starts with property targets [12,62]. To put it another way, the selection of alloying elements for a metallic UHTM cannot be unsystematic or random; instead, it must be coherent and systematic [7,60,62]. Suggestions for research topics that future research could focus on and challenges for alloy designers were discussed in [7,12,46,60,64].

Relationships between solutes, between solutes and parameters, and between parameters, which were reviewed in [12], plus the new relationships that were discussed in this work for the silicide, Laves and A15 phases in the as-cast and heat-treated alloy, and in [46] for the bcc (A2) solid solution and silicide in the alloy NT1.2, plus the new data about the properties of the stable phases in the alloy of this work and in NT1.2 [46], take forward the design of metallic UHTMs along the different "paths" in the "alloy design landscape" shown in Figure 1 in [12]. Synergy, entanglement and self-regulation are key in the NICE "alloy design landscape" that links with risk (IRIS), environment–material interactions (CEMI), material evolution (ETS) and survivability (ESSERE) (see Figures 1 and 2 and Table 1 in [12]). Underlying the complexity of metallic UHTMs is the apparent simplicity of relationships that enable organised complexity to emerge through synergy and entanglement (see Sections 3 and 8 in [12]). In other words, emergence is key to understanding the complexity of metallic UHTMs. In the NICE "alloy design landscape", the processability of metallic UHTMs is not ignored. The aforementioned were briefly discussed in [7], their discussion unfolded in [12] and this paper and [46] have presented new corroborative data. Examples of systematic studies of the processing of metallic UHTMs in our group can be found in [88,89] and in other research groups can be found in [90–96]. The latter form part of the new knowledge and latest knowledge in the NICE "alloy design landscape" (see Figure 1 in [12]).

The alloys NT1.1, NT1.2 [46] and JZ5 [52] (see Appendix A for alloy compositions) had similar chemical compositions and used the same ten solutes, namely Al, Cr, Ge, Hf, Mo, Nb, Si, Sn, Ti and W, but had different stable phases, namely Nb- and W-rich bcc (A2) solid solution, Nb_5Si_3 and $A15–Nb_3X$ in JZ5 [52], Nb- and Mo-rich bcc (A2) solid solution and Nb_5Si_3 in NT1.2 [46] and Nb_5Si_3 and $A15–Nb_3X$ in NT1.1. The design of NT1.2 was guided by data for metallic UHTMs with Ge or Sn or Ge + Sn additions with/without Hf and with/without refractory metals (see the introduction in [46]). The alloy OHS1 [48] with

its seven alloying elements, Al, Cr, Ge, Nb, Si, Sn and Ti, confirmed the importance of the synergy of Ge and Sn with the other solutes regarding ETS and CEMI (see Figure 16 in [60] and Figures 14–16 in [52]). The data for the contaminated with oxygen phases in NT1.2 [46] and for the contaminated with oxygen bcc solid solution in the metallic UHTM that was studied in [42] accentuated the importance of CEMI in alloy design.

In this work, we showed the "evolution" of the microstructure of the alloy NT1.1 at 1500 °C with the VEC versus $\Delta\chi$ maps in Figures 16 and 24a, and the VEC, $\Delta\chi$ and time diagram in Figure 24b. We can use VEC, $\Delta\chi$, E_s, and VEC, $\Delta\chi$, nanoH diagrams to show the properties of phases in an "evolving" microstructure, as shown in Figure 27.
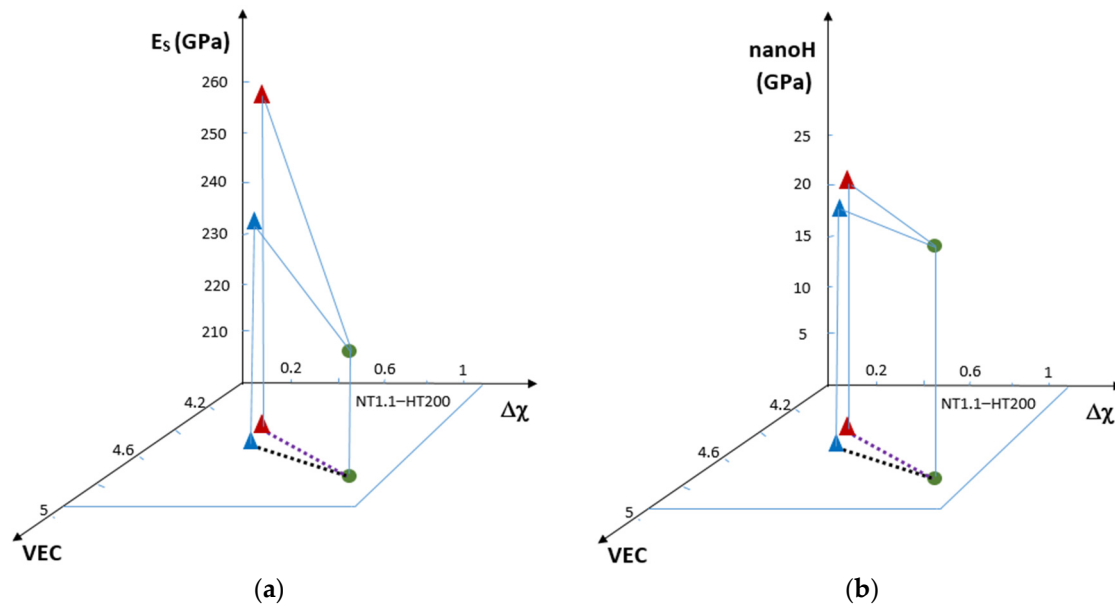
Figure 27. (**a**) VEC, $\Delta\chi$, E_s and (**b**) VEC, $\Delta\chi$, nanoH diagrams of the phases in NT1.1–HT200. For colours and shapes, see the caption of Figure 24b.

The VEC, $\Delta\chi$, time diagram of the alloy NT1.2 for the same temperature, i.e., for 1500 °C, is shown in Figure 28a. In the case of the alloy NT1.2, owing to the precipitation of A2 solid solution in the silicide grains of the heat-treated microstructure, three types of silicide were identified owing to their different chemical composition, namely "core", "boundary" and Ti-rich; see [46]. In other words, the silicide that formed in the as-cast NT1.2, after heat treatment "evolved" into three different types of silicide having different chemical compositions. These are shown with triangle, diamond and square shapes in Figure 28a. The correlations in the VEC versus $\Delta\chi$ maps for the heat-treated alloy NT1.2, which are difficult to show in Figure 28a, are shown in Figure 28b,c.

The phases that formed in the microstructures of the as-cast RCCAs alloys JZ5, NT1.1 and NT1.2 are shown in the VEC versus $\Delta\chi$ map in Figure 29a. For the TM_5Sn_2X compound, see [52,97], the parameter VEC was calculated using $[VEC]_{TM5Sn2X} = \Sigma_i{}^n C_i(VEC)_i$ where C_i and $(VEC)_i$, respectively, are the concentration (at. %) and VEC of element i in the intermetallic and the electronegativity parameter was $[\Delta\chi]_{TM5Sn2X} = \Sigma_i{}^m c_i(\chi <_{Nb}>_i) - \Sigma_i{}^z <\kappa_i(\chi <_{Sn}>_i)$, where c_i and $\chi <_{Nb}>_i$, respectively, are the concentration (at.%) and Pauling electronegativity of Nb and element i substituting Nb in TM_5Sn_2X, and κ_i and $\chi <_{Sn}>_i$, respectively, are the concentration (at.%) and Pauling electronegativity of Sn and element X = Al, Si, Ge. For the other phases, the parameters were calculated as discussed in [44,61]. Figure 29b shows that the phases that form in the as-cast RCCAs alloys JZ5, NT1.1 and NT1.2 with solutes Al, Cr, Ge, Hf, Mo, Nb, Si, Sn, Ti and W are correlated. As solute concentrations changed in the said alloys, the "territory" of each alloy changed in the VEC versus $\Delta\chi$ map; see Figure 29c. The "territory" of NT1.2–AC was the smallest compared with that of JZ5–AC, owing to the largest percentage changes in the solute ratios,

which increased in the heat-treated microstructure; see Table 7. Note that in the heat-treated RCCAs alloys JZ5 and NT1.2, the bcc (A2) solid solution, respectively, was Nb and W, and Nb- and Mo-rich, and that the A15–Nb$_3$X and silicide were correlated; see Figure 30.

(a)

(b)

(c)
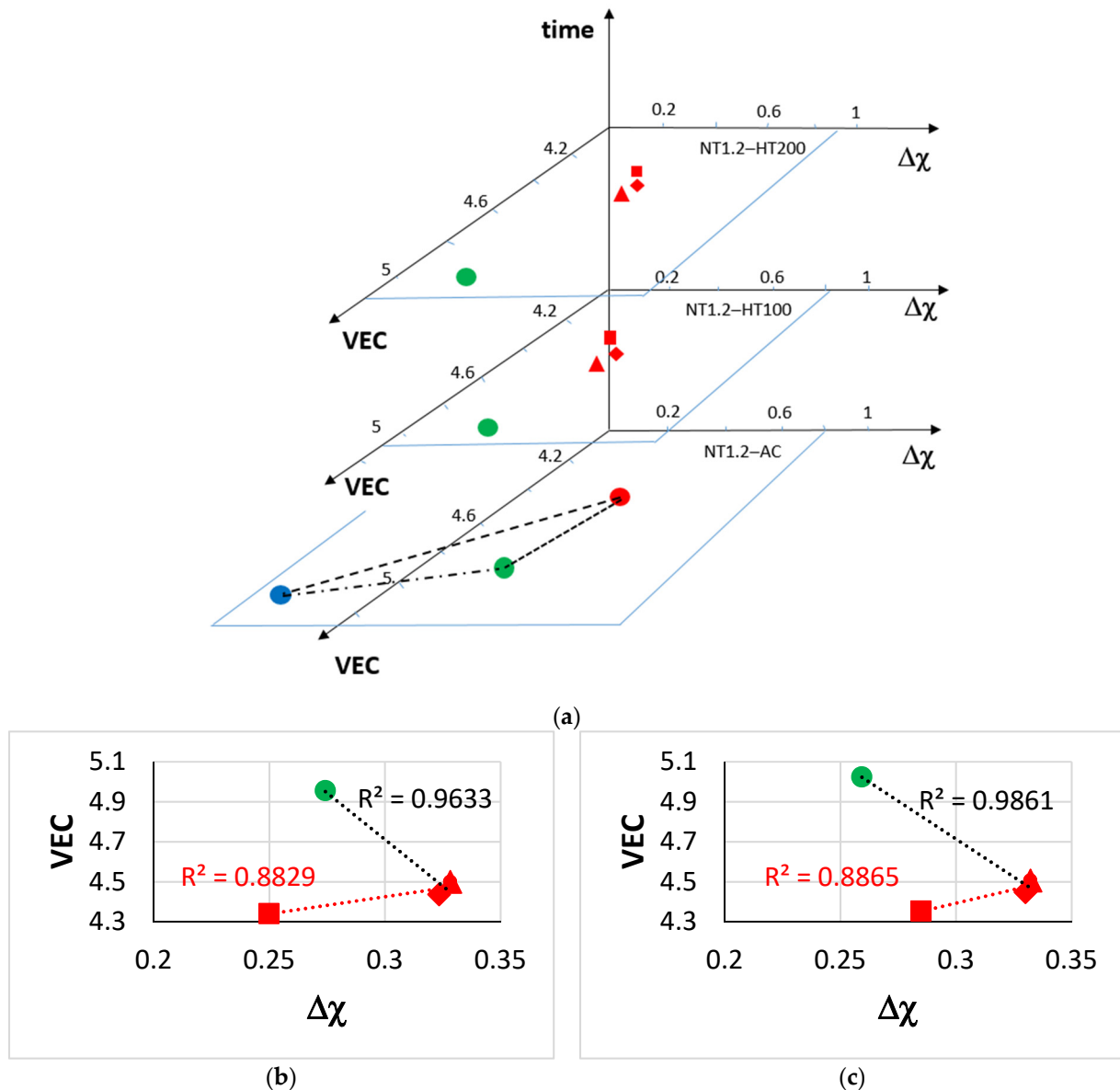
Figure 28. (**a**) VEC, $\Delta\chi$, time diagram of the alloy NT1.2 showing the "evolution" of microstructure at 1500 °C. Colours as follows: blue C14–NbCr$_2$ Laves phase, green A2 solid solution, red Nb$_5$Si$_3$ silicide. (**b**,**c**) VEC versus $\Delta\chi$ maps of phases in NT1.2–HT100 and NT1.2–HT200, respectively. Triangle for the "core" silicide, diamond for the "boundary" silicide, square for the Ti-rich silicide, see text and [46]. (**b**) R^2 = 0.9633 for A2 solid solution and "core" and "boundary" silicide, and R^2 = 0.8829 for "core", "boundary" and Ti-rich silicide. (**c**) R^2 = 0.9861 for A2 solid solution and "core" and "boundary" silicide, and R^2 = 0.8865 for "core", "boundary" and Ti-rich silicide.
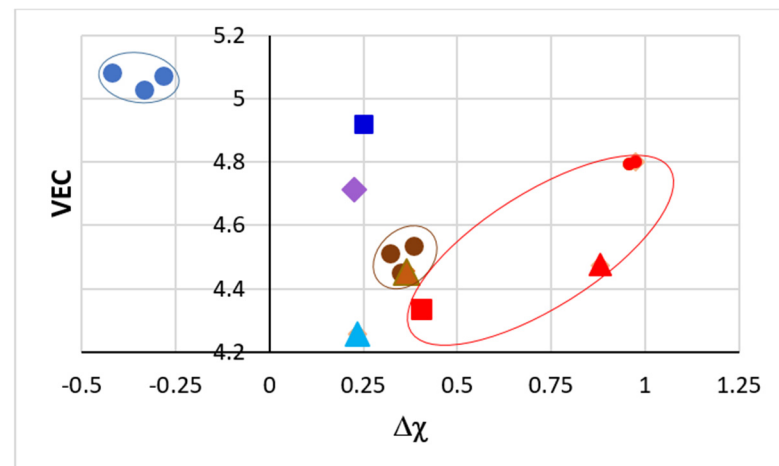
(a)
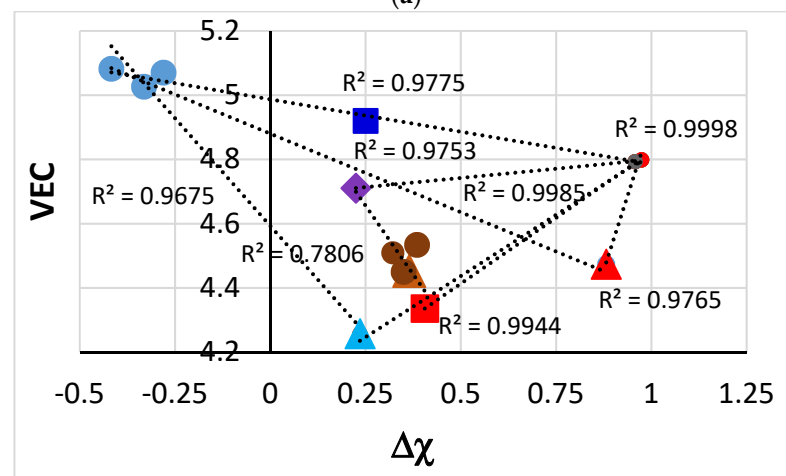
(b)
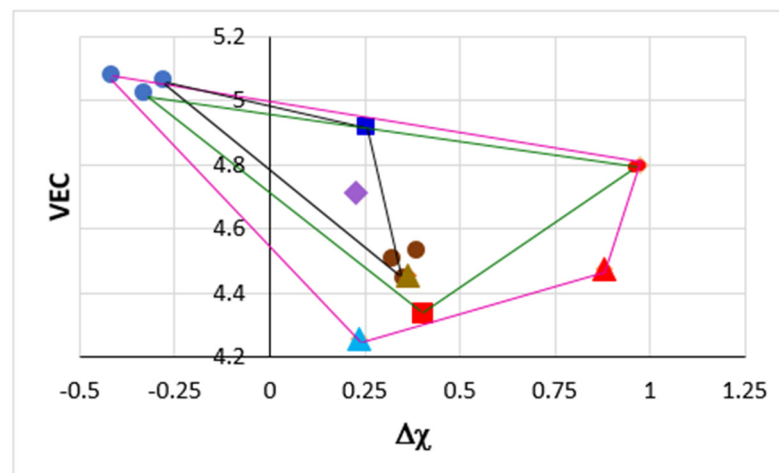
(c)

Figure 29. (**a**) VEC versus Δχ map of phases in the as-cast RCCAs alloys JZ5, NT1.1 and NT1.2 with Al, Cr, Ge, Hf, Mo, Nb, Si, Sn, Ti, W. Shapes and colours as follows: blue filled circles C14–NbCr$_2$-based Laves phase, blue square A2 solid solution, light blue triangle TM$_5$Sn$_2$X, purple diamond eutectic of C14–NbCr$_2$-based Laves phase, A15-Nb$_3$X low <X> and A15-Nb$_3$X high <X> where <X> = Al + Ge + Si + Sn, brown filled circles Nb$_5$Si$_3$, brown triangle Ti-rich Nb$_5$Si$_3$, red square A15–Nb$_3$X high <X>, red circles A15–Nb$_3$X low <X>, red triangle Ti-rich A15–Nb$_3$X. Blue ellipse for C14–NbCr$_2$-based Laves phase "territory", brown ellipse for Nb$_5$Si$_3$ "territory" and red ellipse for

A15–Nb$_3$X "territory". (**b**) The same VEC versus Δχ map showing correlations between phases, as follows: R^2 = 0.9998 for A15–Nb$_3$X high <X> and A15–Nb$_3$X low <X>, R^2 = 0.9985 for eutectic, A15–Nb$_3$X low <X>, R^2 = 0.9944 for TM$_5$Sn$_2$X, A15–Nb$_3$X low <X>, A15–Nb$_3$X high <X>, R^2 = 0.9775 for C14–NbCr$_2$-based Laves phase, A15–Nb$_3$X low <X>, A2 solid solution, R^2 = 0.9765 for Ti-rich A15–Nb$_3$X, A15–Nb$_3$X low <X>, R^2 = 0.9753 for C14–NbCr$_2$-based Laves phase, eutectic, Ti-rich A15–Nb$_3$X, R^2 = 0.9675 for TM$_5$Sn$_2$X and C14–NbCr$_2$ Laves phase, R^2 = 0.9617 for eutectic, C14–NbCr$_2$ Laves phase (line not shown) and R^2 = 0.7806 for eutectic, Nb$_5$Si$_3$ and A15–Nb$_3$X high <X>. (**c**) Pink "territory" JZ5–AC, green "territory" NT1.1–AC, see Figure 16, black "territory" (triangle) NT1.2–AC, see Figure 13a in [46].

Table 7. Solute ratios and percentage change in ratios for the as-cast and heat-treated alloys NT1.1 and NT1.2 with reference, respectively, the as-cast and heat-treated alloy JZ5. TM = Cr + Hf + Ti, RM = Mo + Nb + W, SM = Al + Ge + Si + Sn.

Solute Ratios	Alloy										
	JZ5 AC	JZ5 HT	NT1.1–AC		NT1.1–HT		NT1.2–AC		NT1.2–HT	
(TM + RM)/SM	1.89	1.87	1.97	+4.2%	2	+6.95%	2	+5.8%	2.06	+10.2%
RM/TM	1.52	1.47	1.64	+7.9%	1.69	+15%	1.7	+11.8%	1.84	+25.2%
RM/SM	1.14	1.11	1.23	+7.9%	1.26	+13.5%	1.27	+11.4%	1.33	+19.8%
TM/SM	0.75	0.76	0.75	0%	0.74	−2.6%	0.73	−2.7%	0.72	−5.3%
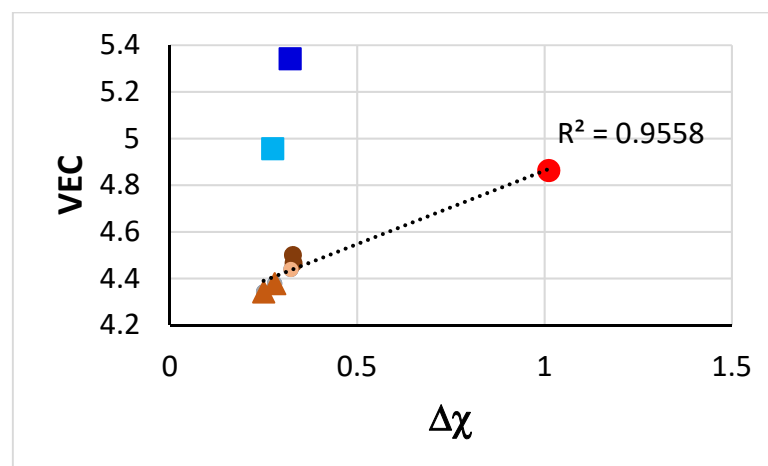
Figure 30. VEC versus Δχ map of phases in the heat-treated RCCAs alloys JZ5 and NT1.2. Shapes and colours as follows: blue data for A2 solid solution, red data for A15–Nb$_3$X, brown data for Nb$_5$Si$_3$, circles for Nb$_5$Si$_3$, triangles for Ti-rich Nb$_5$Si$_3$, light brown circle for "boundary" Nb$_5$Si$_3$ in NT1.2. R^2 = 0.9558 for A15-Nb$_3$X and all Nb$_5$Si$_3$ data. Dark blue for the Nb- and W-rich solid solution (JZ5), light blue for the Nb- and Mo-rich solid solution (NT1.2).

The microstructures of OHS1 [48] and JZ5 [52] drew our attention to the potential of utilising directional solidification (DS) methods for solidification processing [7]. This potential was further supported by the microstructures of NT1.1 and NT1.2. The macrosegregation in OHS1 [48], JZ5 [52], NT1.2 [46] and NT1.1, the correlations between phases in RCCAs with Al, Cr, Ge, Hf, Mo, Nb, Si, Sn, Ti and W solutes (Figure 29b), the VEC, Δχ, time diagrams (Figures 24b and 28a) and the differences regarding the phases in the as-cast microstructures and different stable phases in the said alloys would suggest that with DS, utilising macrosegregation patterns [12] and solidification parameters [88], it should be possible to create microstructures consisting of aforementioned stable phases in different parts of a DS component. In other words, it is suggested that it should be possible to produce DS components with "tailor made" microstructures in different parts of the

component, say an aerofoil. This is a challenge that could be addressed by alloy design, development and solidification processing (see Section 9 in [12]).

The new data in this work and in [46], about how the hardness and Young's moduli of the solid solution, βNb_5Si_3 and A15–Nb_3X, change with different solutes flags poses another challenge for alloy designers, namely, the modelling of microstructures and properties of metallic UHTMs cannot ignore the "dynamics" that result from the synergy and entanglement of solutes and phases not only in defining microstructures but also the properties of coexisting phases, whether these are "conventional", complex concentrated (CC) or high entropy (HE).

5. Conclusions

The stable phases in the RCCA that were studied in this work were the A15-Nb_3X and $D8_m$ βNb_5Si_3 intermetallics. Relationships between solutes, between solutes and the parameters VEC or $\Delta\chi$, and between these parameters for the stable phases and the C14–$NbCr_2$-based laves phase that was formed in the as-cast alloy, the majority of which were reported for the first time in this work for a metallic UHTM, were shown to be important for the development of the alloy microstructure and the properties of its stable phases. The average Young's modulus and nano-hardness values of the stable phases were E_s = 232.6, nanoH = 17.2 for the βNb_5Si_3, and E_s = 204.5, nanoH = 14.7 for the A15–Nb_3X. The Ti-rich silicide had E_s = 258.7 GPa and nanoH = 20.5 GPa. The aforementioned relationships, the VEC versus $\Delta\chi$ maps of the phases in the as-cast and heat-treated alloy, the "evolution" of the alloy parameter map, and the properties of the two stable phases demonstrated the importance of the synergy and entanglement of solutes, parameters and phases in the microstructure and properties of this RCCA.

Abbreviations

AC	as cast
CC	complex concentrated (also compositionally complex)
DS	directional solidification
HE	high entropy
HT	heat treated
NICE	niobium intermetallic composite elaboration
RM	refractory metal
RMIC	refractory metal intermetallic composite
RHEA	refractory metal high-entropy alloy
RCCA	refractory metal complex concentrated alloy
RMIC/RHEA	RMIC that also meets the definition of RHEA
RM(Nb)IC	refractory metal intermetallic composite based on Nb
RM(Nb)IC/RCCA	RM(Nb)IC that also meets the definition of RCCA
RM(Nb)IC/RHEA	RM(Nb)IC that also meets the definition of RHEA

TM	transition metal
UHTM	ultra-high temperature material

Appendix A

Table A1. Alloy Compositions (at.%).

JN1	43Nb–24Ti–18Si–5Al–5Cr–5Hf	[84]
JZ4	38.9Nb–12.5Ti–17.8Si–5Al–5.2Cr–5.2Ge–1.1Hf—–6.2Mo–5.8Sn–2.3W	[52]
JZ5	32Nb–20.4Ti–19.2Si–4.5Al–4.7Cr–5.2Ge–0.9Hf–6.3Mo–5.7Sn–1.1W	[52]
NT1.2	36Nb–20Ti–22Si–3.5Al–4Cr–6Ge–1Hf–5Mo–1.5Sn–1W	[46]
OHS1	38Nb–24Ti–18Si–5Al–5Cr5–Ge–5Sn	[48]

References

1. Jackson, M.R.; Bewlay, B.P.; Rowe, R.G.; Skelly, D.W.; Lipsitt, H.A. High-Temperature Refractory Metal-Intermetallic Composites. *JOM* **1996**, *48*, 39–44. [CrossRef]
2. Subramanian, P.R.; Mendiratta, M.G.; Dimiduk, D.M.; Stucke, M.A. Advanced intermetallic alloys—Beyond gamma titanium aluminides. *Mater. Sci. Eng. A* **1997**, *239*, 1–13. [CrossRef]
3. Balsone, S.J.; Bewlay, B.P.; Jackson, M.R.; Subramanian, P.R.; Zhao, J.C.; Chatterjee, A.; Heffernan, T.M. Materials beyond superalloy-exploiting high temperature composites. In *Structural Intermetallics*; Hemker, K.J., Dimiduk, B.M., Clemens, H., Darolia, R., Inui, M., Larsen, J.M., Sikka, V.K., Thomas, M., Whittenberger, J.D., Eds.; TMS (The Minerals, Metals & Materials Society): Warrendale, PA, USA, 2001; pp. 99–108. ISBN 0-87339-511-5.
4. *Aeronautical Materials for Today and Tomorrow: Following the Forum Organised by the Air and Space Academy (AAE), French Aerospace Society (3AF) and Academy of Technologies, at SAGEM, Paris, 30 November 2012*; AAE-3AF: Toulouse, France; Paris, France, 2014; AAE Dossier #39, 3AF Cahier #10; ISBN 978-2-913331-56-3/979-10-92518-09-2. ISSN 1147-3657.
5. Bewlay, B.P.; Jackson, M.R.; Gigliotti, M.F.X. Niobium silicide high temperature in situ composites. Chapter 6 in Intermetallic Compounds: Principles and Practice. *Intermet. Compd. Princ. Pract.* **2002**, *3*, 541–560.
6. Bewlay, B.P.; Jackson, M.R.; Subramanian, P.R.; Lewandowski, J.J. Very high temperature Nb silicide based composites. In *Niobium for High Temperature Applications*; Kim, Y.-W., Carneiro, T., Eds.; TMS (The Minerals, Metals & Materials Society): Warrendale, PA, USA, 2004; pp. 51–61.
7. Tsakiropoulos, P. Alloys for application at ultra-high temperatures: Nb-silicide in situ composites: Challenges, breakthroughs and opportunities. *Prog. Mater. Sci.* **2022**, *123*, 100714. [CrossRef]
8. Bewlay, B.P.; Jackson, M.R.; Subramanian, P.R.; Zhao, J.-C. A review of very-high-temperature Nb-silicide-based composites. *Metall. Mater. Trans. A* **2003**, *34*, 2043–2052. [CrossRef]
9. Bewlay, B.P.; Jackson, M.R.; Zhao, J.-C.; Subramanian, P.R.; Mendiratta, M.G.; Lewandowski, J.J. Ultra-high temperature Nb-silicide based composites. *MRS Bull.* **2003**, *28*, 646–653. [CrossRef]
10. Senkov, O.N.; Miracle, D.B.; Chaput, K.J. Development and exploration of refractory High entropy alloys—A review. *J. Mater. Res.* **2018**, *33*, 3092–3128. [CrossRef]
11. Mitrica, D.; Badea, I.C.; Serban, B.A.; Olaru, M.T.; Vonica, D.; Burada, M.; Piticescu, R.-R.; Popov, V.V. Complex Concentrated Alloys for Substitution of Critical Raw Materials in Applications for Extreme Conditions. *Materials* **2021**, *14*, 1197. [CrossRef]
12. Tsakiropoulos, P. A Perspective of the Design and Development of Metallic Ultra-High Temperature Materials: Refractory Metal Intermetallic Composites, Refractory Complex Concentrated Alloys and Refractory High Entropy Alloys. *Alloys* **2023**, *2*, 184–212. [CrossRef]
13. Xu, Z.Q.; Ma, Z.L.; Tan, Y.; Wang, M.; Zhao, Y.; Cheng, X.W. Cheng. Effects of Si additions on microstructures and mechanical properties of VNbTiTaSix refractory high-entropy alloys. *J. Alloys Compd.* **2022**, *900*, 163517. [CrossRef]
14. Pei, X.; Du, Y.; Wang, H.; Hu, M.; Wang, H.; Liu, W. Investigation of high temperature tribological performance of TiZrV0. 5Nb0. 5 refractory high-entropy alloy optimized by Si microalloying. *Tribol. Int.* **2022**, *176*, 107885. [CrossRef]
15. Fan, Z.; Niu, B.; Wang, Q.; Sha, J.; Dong, C. Effects of Si variation and Zr addition on the microstructure, oxidation resistance and mechanical property at 1523 K of Nb-Si-Ti/Zr/Hf-Cr/Al high-entropy superalloys. *J. Alloys Compd.* **2023**, *945*, 169304. [CrossRef]
16. Chan, K.S. *Optimisation of Niobium Based In Situ Composites for High Temperature Applications*; AFOSR Final Report Under Contract F49620-01-C-0016; Southwest Research Institute: Washington, DC, USA, 2003.
17. Guo, H.; Guo, X. Microstructure evolution and room temperature fracture toughness of an integrally directionally solidified Nb-Ti-Si based ultrahigh temperature alloys. *Scr. Mater.* **2011**, *64*, 637–640. [CrossRef]
18. Wang, Q.; Zhou, C.; Wang, S.; Chen, R. Effect of Zr and Hf additions on microstructure and mechanical properties of Nb–Si based ultrahigh temperature alloys. *J. Mater. Res. Technol.* **2020**, *9*, 15585–15592. [CrossRef]
19. Shen, F.; Zhang, Y.; Yu, L.; Fu, T.; Wang, J.; Wang, H.; Cui, K. Microstructure and oxidation behaviour of Nb-Si-based alloys for ultrahigh temperature applications: A comprehensive review. *Coatings* **2021**, *11*, 1373. [CrossRef]
20. Wang, Y.; Jia, L.; Ye, C.; Zhang, H. Enhanced room temperature fracture toughness of directionally solidified Nbss/Nb5Si3 in situ composites via Rhenium addition. *J. Mater. Res. Technol.* **2022**, *20*, 2758–2770. [CrossRef]

21. Kommineni, G.; Golla, B.R.; Prasad, V.V. An Overview on Effect of Alloying Elements on the Phase Formation, Mechanical and Oxidation Properties of Nb-Nb Silicide In Situ Composites. *Silicon* **2023**, *15*, 651–681. [CrossRef]

22. Tang, Y.; Xiao, B.; Chen, J.; Liu, F.; Du, W.; Guo, J.; Liu, Y.; Liu, Y. Multi-component Alloying Effects on the Stability and Mechanical Properties of Nb and Nb–Si Alloys: A First-Principles Study. *Metall. Mater. Trans. A* **2023**, *54*, 450–472. [CrossRef]

23. Yeh, J.W. Alloy Design Strategies and Future Trends in High-Entropy Alloys. *JOM* **2013**, *65*, 1759–1771. [CrossRef]

24. Tsai, M.-H.; Yeh, J.-W. High-Entropy Alloys: A Critical Review. *Mater. Res. Lett.* **2014**, *2*, 107–123. [CrossRef]

25. Wei, X.; Olson, G.B. Integrated computational materials design for high-performance alloys. *MRS Bull.* **2015**, *40*, 1035–1044.

26. Guo, N.N.; Wang, L.; Luo, L.S.; Li, X.Z.; Chen, R.R.; Su, Y.Q.; Guo, J.J.; Fu, H.Z. Microstructure and mechanical properties of refractory high entropy ($Mo_{0.5}NbHf_{0.5}ZrTi$)BCC/M_5Si_3 in-situ compound. *J. Alloy. Compd.* **2016**, *660*, 197–203. [CrossRef]

27. Srikanth, M.; Annamalai, A.R.; Muthuchamy, A.; Jen, C.-P. A Review of the Latest Developments in the Field of Refractory High-Entropy Alloys. *Crystals* **2021**, *11*, 612. [CrossRef]

28. Zhou, J.-L.; Cheng, Y.-H.; Chen, Y.-X.; Liang, X.-B. Composition design and preparation process of refractory high-entropy alloys: A review. *Intern. J. Refract. Met. Hard Mater.* **2022**, *105*, 105836. [CrossRef]

29. Dasari, S.; Soni, V.; Sharma, A.; Senkov, O.N.; Miracle, D.B.; Fraser, H.L.; Wang, Y.; Banerjee, R. Concomitant Clustering and Ordering Leading to B2 + BCC Microstructures in Refractory High Entropy Alloys. *Trans. Indian Inst. Met.* **2022**, *75*, 907–916. [CrossRef]

30. Tian, Y.-S.; Zhou, W.-Z.; Tan, Q.-B.; Wu, M.-X.; Qiao, S.; Zhu, G.-L.; Dong, A.-P.; Shu, D.; Sun, B.-D. A review of refractory high-entropy alloys. *Trans. Nonferrous Met. Soc. China* **2022**, *32*, 3487–3515. [CrossRef]

31. Huang, W.; Hou, J.; Wang, X.; Qiao, J.; Wu, Y. Excellent room-temperature tensile ductility in as-cast $Ti_{37}V_{15}Nb_{22}Hf_{23}W_3$ refractory high entropy alloys. *Intermetallics* **2022**, *151*, 107735. [CrossRef]

32. Xu, Z.Q.; Ma, Z.L.; Tan, Y.; Cheng, X.W. Designing TiVNbTaSi refractory high-entropy alloys with ambient tensile ductility. *Scr. Mater.* **2022**, *206*, 114230. [CrossRef]

33. Wang, Z.; Zhang, S. Research and Application Progress of High-Entropy Alloys. *Coatings* **2023**, *13*, 1916. [CrossRef]

34. Chen, C.-L.; Lin, J.-H. Effects of Alloying Elements and Mechanical Alloying on Characteristics of WVTaTiCr Refractory High-Entropy Alloys. *Materials* **2023**, *16*, 6194. [CrossRef]

35. San, S.; Hasan, S.; Adhikari, P.; Ching, W.-Y. Designing Quaternary and Quinary Refractory-Based High-Entropy Alloys: Statistical Analysis of Their Lattice Distortion, Mechanical, and Thermal Properties. *Metals* **2023**, *13*, 1953. [CrossRef]

36. Liu, Z.; Shi, X.; Zhang, M.; Qiao, J. Development of Refractory High Entropy Alloys with Tensile Ductility at Room Temperature. *Metals* **2023**, *13*, 329. [CrossRef]

37. Liang, Z.; Wu, Y.; Miao, Y.; Pan, W.; Zhang, Y. Composition Design and Tensile Properties of Additive Manufactured Low Density Hf−Nb−Ta−Ti−Zr High Entropy Alloys Based on Atomic Simulations. *Materials* **2023**, *16*, 4039. [CrossRef]

38. Moussa, M.; Gorsse, S.; Huot, J.; Bobet, J.L. Effect of the Synthesis Route on the Microstructure of $Hf_xTi_{(1−x)}$NbVZr Refractory High-Entropy Alloys. *Metals* **2023**, *13*, 343. [CrossRef]

39. Guo, Y.; Peng, J.; Peng, S.; An, F.; Lu, W.; Li, Z. Improving oxidation resistance of TaMoZrTiAl refractory high entropy alloys via Nb and Si alloying. *Corros. Sci.* **2023**, *223*, 111455. [CrossRef]

40. Liu, B.; Li, J.; Peterlechner, M.; Zhang, H.; Wu, Y.; Wilde, G.; Ye, F. Microstructure and mechanical properties of Si micro-alloyed $(Ti_{28}Zr_{40}Al_{20}Nb_{12})_{100−x}Si_x$ (x = 0, 0.1, 0.2, 0.5) high entropy alloys. *Intermetallics* **2023**, *161*, 107959. [CrossRef]

41. Chen, Y.; Gao, X.; Qin, G.; Chen, R.; Guo, J. Achieving excellent specific yield strength in non-equiatomic TiNbZrVMo high entropy alloy via metalloid Si doping. *Mater. Lett.* **2023**, *335*, 133832. [CrossRef]

42. Tsakiropoulos, P. On the Stability of Complex Concentrated (CC)/High Entropy (HE) Solid Solutions and the Contamination with Oxygen of Solid Solutions in Refractory Metal Intermetallic Composites (RM(Nb)ICs) and Refractory Complex Concentrated Alloys (RCCAs). *Materials* **2022**, *15*, 8479. [CrossRef] [PubMed]

43. Tsakiropoulos, P. On the Nb_5Si_3 Silicide in Metallic Ultra-High Temperature Materials. *Metals* **2023**, *13*, 1023. [CrossRef]

44. Tsakiropoulos, P. Alloying and Properties of $C14–NbCr_2$ and $A15–Nb_3X$ (X = Al, Ge, Si, Sn) in Nb–Silicide-Based Alloys. *Materials* **2018**, *11*, 395. [CrossRef]

45. Tsakiropoulos, P. Alloying and Hardness of Eutectics with Nb_{ss} and Nb_5Si_3 in Nb-silicide Based Alloys. *Materials* **2018**, *11*, 592. [CrossRef] [PubMed]

46. Tankov, N.; Utton, C.; Tsakiropoulos, P. On the Microstructure and Properties of Complex Concentrated bcc Solid Solution and Tetragonal $D8_m$ M_5Si_3 Silicide Phases in a Refractory Complex Concentrated Alloy. *Alloys* **2024**, *3*, 59–95. [CrossRef]

47. Zacharis, E.; Utton, C.; Tsakiropoulos, P. A Study of the Effects of Hf and Sn on the Microstructure, Hardness and Oxidation of Nb-18Si Silicide-Based Alloys-RM(Nb)ICs with Ti Addition and Comparison with Refractory Complex Concentrated Alloys (RCCAs). *Materials* **2022**, *15*, 4596. [CrossRef]

48. Hernandez-Negrete, O.; Tsakiropoulos, P. On the microstructure and isothermal oxidation at 800 and 1200 °C of the Nb-24Ti-18Si5Al-5Cr-5Ge-5Sn (at.%) silicide based alloy. *Materials* **2020**, *13*, 722. [CrossRef]

49. Li, Z.; Tsakiropoulos, P. On the microstructure and hardness of the Nb-24Ti-18Si-5Al-5Cr-5Ge and Nb-24Ti-18Si-5Al-5Cr-5Ge-5Hf (at.%) silicide based alloys. *Materials* **2019**, *12*, 2655. [CrossRef] [PubMed]

50. Schlesinger, M.E.; Okamoto, H.; Gokhale, A.B.; Abbaschian, R. The Nb-Si (Niobium-Silicon) System. *J. Phase Equilibria* **1993**, *14*, 502–509. [CrossRef]

51. Bewlay, B.P.; Sitzman, S.D.; Brewer, L.N.; Jackson, M.R. Analyses of eutectoid phase transformations in Nb-silicide in-situ composites. *Microsc. Microanal.* **2004**, *10*, 470–480. [CrossRef] [PubMed]

52. Zhao, J.; Utton, C.; Tsakiropoulos, P. On the Microstructure and Properties of Nb-18Si-6Mo-5Al-5Cr-2.5W-1Hf Nb-Silicide Based Alloys with Ge, Sn and Ti Additions (at.%). *Materials* **2020**, *13*, 4548. [CrossRef]

53. Goldschmidt, H.J.; Brand, J.A. The constitution of the niobium-chromium-silicon system. *J. Less Common Met.* **1961**, *3*, 34–43. [CrossRef]

54. Zhao, J.-C.; Jackson, M.R.; Peluso, L.A. Determination of the Nb-Cr-Si phase diagram using diffusion multiples. *Acta Mater.* **2003**, *51*, 6395–6405. [CrossRef]

55. Yang, Y.; Chang, Y.A. Thermodynamic modelling of Nb–Cr–Si system. *Intermetallics* **2005**, *13*, 69–78. [CrossRef]

56. Bewlay, B.P.; Yang, Y.; Casey, R.L.; Jackson, M.R.; Chang, Y.A. Experimental study of the liquid-solid phase equilibria at the metal rich region of the Nb-Cr-Si system. *Intermetallics* **2009**, *17*, 120–127. [CrossRef]

57. Hunt, C.R.; Raman, A. Alloy Chemistry of (U)-Related Phases. *Z. Metallkd.* **1968**, *59*, 701–707.

58. Mahdouk, K.; Gachon, J.C. A Thermodynamic Study of the Al-Cr-Nb Ternary System. *J. Alloys Compd.* **2001**, *321*, 232–236. [CrossRef]

59. Zhao, J.C.; Jackson, M.R.; Peluso, L.A. Evaluation of phase relations in the Nb-Cr-Al sytem at 1000 °C using diffusion-multiple approach. *J. Phase Equilibria Diffus.* **2004**, *25*, 152–159.

60. Tsakiropoulos, P. Refractory Metal (Nb) Intermetallic Composites, High Entropy Alloys, Complex Concentrated Alloys and the Alloy Design Methodology NICE—Mise-en-scène Patterns of Thought and Progress. *Materials* **2021**, *14*, 989. [CrossRef]

61. Tsakiropoulos, P. On the alloying and properties of tetragonal Nb_5Si_3 in Nb-silicide Based Alloys. *Materials* **2018**, *11*, 69. [CrossRef]

62. Tsakiropoulos, P. On Nb Silicide Based Alloys: Alloy Design and Selection. *Materials* **2018**, *11*, 844. [CrossRef]

63. Tsakiropoulos, P. On Nb Silicide Based alloys: Part II. *J. Alloys Compd.* **2018**, *748*, 569–576. [CrossRef]

64. Tsakiropoulos, P. Refractory Metal Intermetallic Composites, High-Entropy Alloys, and Complex Concentrated Alloys: A Route to Selecting Substrate Alloys and Bond Coat Alloys for Environmental Coatings. *Materials* **2022**, *15*, 2832. [CrossRef]

65. Oliver, W.C.; Pharr, G.M. An improved technique for determining hardness and elastic modulus Using load and displacement sensing indentation experiments. *J. Mater. Res.* **1992**, *7*, 1564–1583. [CrossRef]

66. *Triboscope User Manual*; Hysitron Ltd.: Eden Prairie, MN, USA, 2005.

67. Papadimitriou, I.; Utton, C.; Scott, A.; Tsakiropoulos, P. Ab Initio study of binary and ternary $Nb_3(X,Y)$ A_{15} intermetallic phases (X,Y = Al, Ge, Si, Sn). *Metall. Mater. Trans. A* **2015**, *46*, 566–576. [CrossRef]

68. Papadimitriou, I.; Utton, C.; Tsakiropoulos, P. The impact of Ti and temperature on the stability of Nb_5Si_3 phases: A first-principles study. *Sci. Technol. Adv. Mater.* **2017**, *18*, 467–479. [CrossRef] [PubMed]

69. Chen, Y.; Hammerschmidt, T.; Pettifor, D.G.; Shang, J.; Zhang, Y. Influence of vibrational entropy on structural stability of Nb-Si and Mo-Si systems at elevated temperatures. *Acta Mater.* **2009**, *57*, 2657–2664. [CrossRef]

70. Shi, S.; Zhu, L.; Jia, L.; Zhang, H.; Sun, Z. Ab initio study of alloying effects on structure stability and mechanical properties of Nb_5Si_3. *Comput. Mater. Sci.* **2015**, *108*, 121–127. [CrossRef]

71. MSundareswari; Ramasubramanian, S.; Rajagopalan, M. Elastic and thermodynamical properties of A15 Nb_3X (X = Al, Ga, In, Sn and Sb) compounds—First principles DFT study. *Solid State Commun.* **2010**, *150*, 2057–2060. [CrossRef]

72. Old, C.F.; Charlesworth, J.P. The breaking strain of Nb_3Sn in a multi-filamentary superconductor. *Cryogenics* **1976**, *16*, 469. [CrossRef]

73. Koch, C.C.; Easton, D.S. *Mechanical Behaviour and Stress Effects in Hard Superconductors—A Review*; under Contract No. W-7405-eng-26, ORNL/TM-5857 Dist. Category UC-2; Oak Ridge National Laboratory: Oak Ridge, TN, USA, 1977.

74. Persson, K. Materials Data on AlMo3 (SG:223) by Materials Project. February 2016. An Optional Note. Available online: https://legacy.materialsproject.org/materials/mp-259/ (accessed on 18 January 2024). [CrossRef]

75. Zhong, S.-Y.; Chen, Z.; Wang, M.; Chen, D. Structural, elastic and thermodynamic properties of Mo_3Si and Mo_3Ge. *Eur. Phys. J. B* **2016**, *89*, 6. [CrossRef]

76. HTutuncu, M.; Bagci, S.; Srivastava, P. Electronic structure, phonons, and electron-phonon interaction in Mo_3Si. *Phys. Rev. B* **2010**, *82*, 214510. [CrossRef]

77. Ma, N.; Cooper, B.R.; Kang, B.S. Tight-binding study of thermal expansions for Mo_3Si. *J. Appl. Phys.* **2006**, *99*, 053514. [CrossRef]

78. Xu, J.; Li, Z.; Lu, X.; Yan, Y.; Munroe, P.; Xie, Z.-H. Mechanical and electrochemical properties of nanocrystalline $(Mo_{1-x}Cr_x)_3Si$ coatings: Experimental and modelling studies. *J. Alloy. Compd.* **2014**, *611*, 179–190. [CrossRef]

79. Biragoni, P.G.; Heilmaier, M. Fem-simulation of real and artificial microstructures of Mo-Si-B alloys for elastic properties and comparison with analytical methods. *Adv. Eng. Mater.* **2007**, *9*, 882–887. [CrossRef]

80. Rosales, I.; Schneibel, J.H. Stoichiometry and Mechanical Properties of Mo_3Si. *Intermetallics* **2000**, *8*, 885–889. [CrossRef]

81. Bi, W.; Sun, S.; Bei, S.; Jiang, Y. Effect of Alloying Elements on the Mechanical Properties of Mo_3Si. *Metals* **2021**, *11*, 129. [CrossRef]

82. Pudasaini, U.; Eremeev, G.V.; Cheban, S. First Results From Nanoindentation of Vapor Diffused Nb_3Sn Films on Nb. In Proceedings of the 21st International Conference on Radio-Frequency Superconductivity (SRF 2023), Grand Rapids, MI, USA, 25–30 June 2023; JACoW: Geneva, Switzerland, 2023; pp. 888–5504. [CrossRef]

83. Rehwald, W.; Rayl, M.; Cohen, R.W.; Cody, G.D. Elastic Moduli and Magnetic Susceptibility of Monocrystalline Nb_3Sn. *Phys. Rev. B* **1972**, *6*, 363. [CrossRef]

84. Nelson, J.; Ghadyani, M.; Utton, C.; Tsakiropoulos, P. A Study of the Effects of Al, Cr, Hf, and Ti Additions on the Microstructure and Oxidation of Nb-24Ti-18Si Silicide Based Alloys. *Materials* **2018**, *11*, 1579. [CrossRef]

85. Li, Z.; Luo, L.; Wang, B.; Su, B.; Luo, L.; Wang, L.; Su, Y.; Guo, J.; Fu, H. Effect of Ge addition on microstructural evolution and mechanical properties of quinary Nb-16Si-22Ti-2Al-2Cr alloy. *Int. J. Refract. Met. Hard Mater.* **2023**, *116*, 106327. [CrossRef]

86. Chen, X.; Niu, H.; Li, D.; Li, Y. Modelling hardness of polycrystalline materials and bulk metallic glasses. *Intermetallics* **2011**, *19*, 1275–1281. [CrossRef]

87. Tsakiropoulos, P. On the Nb silicide based alloys: Part I—The bcc Nb solid solution. *J. Alloy. Compd.* **2017**, *708*, 961–971. [CrossRef]

88. McCaughey, C.; Tsakiropoulos, P. Type of Primary Nb_5Si_3 and Precipitation of Nb_{ss} in αNb_5Si_3 in a Nb-8.3Ti-21.1Si-5.4Mo-4W-0.7Hf (at.%) Near Eutectic Nb-Silicide-Based Alloy. *Materials* **2018**, *11*, 967. [CrossRef]

89. Graham, S.J.; Gallagher, E.; Baxter, G.J.; Azakli, Y.; Weeks, J.; Gelmetti, M.; D'Souza, N.; Boettcher, C.; Roebuck, B.; Tsakiropoulos, P.; et al. Powder production, FAST processing and properties of a Nb-silicide based alloy for high temperature aerospace applications. *J. Mater. Res. Technol.* **2024**, *28*, 3217–3224. [CrossRef]

90. Yeh, C.L.; Chen, W.H. A Comparative Study on Combustion Synthesis of Nb-Si Compounds. *J. Alloys Compd.* **2006**, *425*, 216–222. [CrossRef]

91. Yi, D.Q.; Li, D.; Li, J.; Zhou, H.M. Powder Metallurgic Process for Preparing Nb-15Ti-11Al-10Si Composites. *Chin. J. Rare Met.* **2007**, *31*, 472–476.

92. Guo, X.P.; Guo, H.S.; Yao, C.F. Integrally Directionally Solidified Microstructure of an Niobium Silicide Based Ultrahigh Temperature Alloy. *Int. J. Mod. Phys. B* **2009**, *23*, 1093–1098. [CrossRef]

93. Lu, Y.Y.; Zhang, J.; Tian, L.X.; Li, Y.L.; Ma, C.L. Microstructural Evolution of Unidirectionally Solidified Nb_{ss}-Nb_5Si_3 Eutectic Alloy. *Rare Met.* **2011**, *30*, 335–339. [CrossRef]

94. Fang, X.; Guo, X.; Qiao, Y. Microstructural transition of Nb-Si based alloy during directional solidification upon abruptly decreasing withdrawal rate. *J. Alloys Compd.* **2020**, *843*, 156073. [CrossRef]

95. Tang, Y.; Guo, X. Role of deformation temperature and strain rate on microstructure evolution of hot compressed Nb-Si based ultra-high temperature alloy. *Intermetallics* **2020**, *119*, 106719. [CrossRef]

96. Zhang, L.; Guan, P.; Guo, X. Microstructure, Mechanical Properties and Oxidation Resistance of Nb-Si Based Ultra high Temperature Alloys Prepared by Hot Press Sintering. *Materials* **2023**, *16*, 3809. [CrossRef]

97. Papadimitriou, I.; Utton, C.; Tsakiropoulos, P. Ab Initio Study of Ternary W_5Si_3 Type TM_5Sn_2X Compounds (TM = Nb, Ti and X = Al, Si). *Materials* **2019**, *12*, 3217. [CrossRef]